Proper orthogonal decomposition analysis of turbulent natural convection in an air-water system with evaporation across the free surface

Julien Carlier[a,*], Bérengère Podvin[b], Miltiadis V. Papalexandris[a]

[a]*Institute of Mechanics, Materials and Civil Engineering, Université catholique de Louvain, 1348 Louvain-la Neuve, Belgium*
[b]*EM2C, CentraleSupélec, CNRS, Université Paris-Saclay, 91190 Gif-sur-Yvette, France*

Abstract

In this paper, we analyze the properties of turbulent natural convection in a water-air system via Proper Orthogonal Decomposition (POD). The flow domain is an open-top cuboid uniformly heated from below, while the water and air are separated by an evaporative interface. Direct numerical simulations of this problem were presented in an earlier publication of ours; herein we investigate in detail the emerging flow structures and the interaction between the two phases. In the water, the flow is organized around a dominant convective roll. In the gas the flow is due to combined thermal-concentration convection. The flow pattern is more complex and consists of an outer circulation plus an inner dual-roll structure with one roll above the other. First we discuss spectra of the thermal fluctuations. In the gas, the spectrum is bimodal. The high-frequency peak is due to natural convection while the low-frequency one is due to the interaction with water at the free surface. Then, we present the results of our POD analysis and elaborate on the properties of the dominant spatial and temporal modes. The spectra of the temporal modes are also examined herein. Our analysis shows that there is high correlation and coherence between the low-frequency signals in the dominant modes of the two phases, which implies that the convective patterns in the two phases influence each other. We also present the reconstructed snapshots with the dominant POD modes and discuss their influence. Our analysis shows that they provide a fairly accurate approximation of the instantaneous flow patterns. Further, in the water, the dominant mode modifies the length of the main convective roll, whereas the second mode tends to rotate its impingement point.

Keywords: natural convection, low-Mach number flow, thermal-concentration convection, evaporation, turbulent convection, proper orthogonal decomposition

1. Introduction

The purpose of this paper is to analyze the flow structures of natural convection in two superimposed columns of liquid water and humid air that are separated by an evaporative interface (the free surface of the water). In such systems, due to the evaporation across the free surface. a temperature gradient arises in the liquid and convection motions are developed; this phenomenon is known as evaporative cooling

*Corresponding author: email julien.carlier@uclouvain.be;

[56, 65]. However, the case considered herein does not fall into this category; instead, heat is added from below and evacuated primarily from above and secondarily at the free surface via evaporation. Such flows are commonly encountered in nature; for example in lakes and seas [13]. They also occur in technological applications and industrial processes, for example in boilers, power plants and spent-fuel pools in nuclear power stations [8]. In such systems, convection is established in both phases and the emerging flow patterns in each phase bear similarities to the classical Rayleigh-Bénard Convection (RBC), *i.e.* convection of a single fluid between two horizontal walls that is heated from below. Nonetheless, the evaporation process and the flow structures in the two phases influence one another.

Over the years, several studies have been devoted to convection in gas-liquid systems. For example, experiments and numerical simulations of two-layer Rayleigh-Bénard convection (two immiscible fluids in a box) with and without phase change have been presented in the recent papers [28, 29, 48, 64]. Nonetheless, thermal convection in gas-liquid systems in open-top containers, such as pools and cavities, has been studied to a much lesser extent. Most efforts on this topic were focused on the evaporation across the free surface. For example, Quinn Brewster [8] proposed a model for the evaporation rate across the free surface and applied it to study convection in spent-fuel pools. Also, Martin et al. [36] provided measurements of the evaporation rate as a function of the free-surface temperature and derived an evaporation model as well.

Direct Numerical Simulations (DNS) of turbulent convection in cavities [36] filled with water were performed in [18, 20]. Therein, the free surface (top boundary) was approximated as a free-slip plane and the evaporation rate was calculated by applying the evaporation model of [36]. Those works examined the dependence of the evaporative flux on the free-surface temperature and also provided correlations between the Nusselt and Rayleigh numbers. However, the convective and transport phenomena that occur in the air above the water were not taken into account. These phenomena, however, are expected to have an influence on the evaporation rate. Similarly, the simulation time was limited so as to keep small the descent of the free surface and the loss of water due to evaporation.

In fact, in the problem of interest, the liquid and gas phases and the free surface constitute three coupled systems whose dynamics have to be solved simultaneously. To this end, in [10] the first and third authors proposed a numerical scheme that solves simultaneously for the flow in both phases and computes dynamically the evaporation rate and the free-surface descent. Subsequently, they employed this scheme to study numerically natural convection in water/air systems at different Rayleigh numbers [11]. One of the findings of that study was that the impingement points of the large-scale circulations at the two sides of the free surface are kept in proximity, which suggests that there is a certain degree of correlation between the convective rolls in the two phases and that these rolls influence one another.

In this paper, we extend the work [11] and present a detailed analysis of the emerging turbulent struc-

tures below and above the free surface. Our analysis is based on the Proper Orthogonal Decomposition (POD). This is a popular statistical technique that was first applied in turbulent flows by Lumley [31, 32]. It allows to extract from an unsteady flow the coherent structures that compose it. These structures, or modes, are ordered in terms of their energies. It is then possible to study the most energetic modes to identify important flow features thus providing additional physical insight.

Over the years, POD has been employed in a variety of fluid-flow problems. For example, it was employed in [5, 14, 45, 61] for RBC in cuboids of low aspect ratio and in [3] for RBC in cylinders of high aspect ratio. An important advantage of this technique is that the modes thus obtained can be used to construct reduced models. Indeed, POD-based reduced modeling in RBC was presented in [46, 47, 54]. Also, [55] presented reduced modeling of RBC coupled with radiation. POD has also been successfully applied in the study of multiphase flows. For instance, it was employed in [37, 38] to study the modes in slug flows. It was also used in porous media: in [15] to investigate the turbulent boundary layer in fishing nets and in [27] for reduced-order modeling. Yet another example of the application of POD is bubbly flow [40, 63] in which the authors studied the effects of the bubbles on turbulent structures.

With regard to the configuration of interest, in this paper we consider a cuboid with an open-top boundary in contact with atmospheric air. The vertical walls are adiabatically isolated and the bottom wall is heated from below. The lower part of the cuboid contains liquid water and is referred to as the water column. While the upper part contains humid air and is referred to as the gas column. The two columns are separated by an interface (the free surface of the water) across which liquid water evaporates. Hereafter we will use the terms *interface* and *free surface*. interchangeably.

Due to the difference of temperatures at the bottom and the top boundaries, thermal convection is established in both columns. For the flow in hand we perform DNS based on the solver [10] and then apply POD in the numerical results. Herein, we discuss and analyze both the temporal and the spatial modes. Particular emphasis is placed on the influence of the dominant modes in the water to those in the gas. Additionally, we reconstruct the flow in the two columns with the most dominant modes in the two columns and elaborate on their effects on the flow.

This paper is structured as follows. In section 2 we present the governing equations and the jump relations of the problem of interest. In section 3 we outline the main steps of POD. In section 4 we first explain the numerical setup of the simulation. Then, we discuss the main properties and characteristics of the flow patterns in the two phases and analyze the spectrum of the thermal fluctuations in each phase. In section 5, we present the results of our POD analysis. Finally, section 6 concludes.

2. Mathematical model

2.1. Governing equations

We consider an open-top water, partially filled with liquid water. The part of the cuboid above the water is filled with humid air. The two phases are separated by an interface, *i.e.* the free surface of the water. The governing system of equations is the low-Mach number approximation of the compressible Navier-Stokes-Fourier equations [26, 41],

$$\frac{\partial \rho}{\partial t} + \nabla \cdot (\rho \boldsymbol{u}) = 0, \tag{1}$$

$$\frac{\partial \rho \boldsymbol{u}}{\partial t} + \nabla \cdot (\rho \boldsymbol{u}\boldsymbol{u}) = -\nabla p' + \nabla \cdot (\mu \boldsymbol{S}) + g y \nabla \rho, \tag{2}$$

$$c_p \frac{\partial \rho T}{\partial t} + c_p \nabla \cdot (\rho \boldsymbol{u} T) = \frac{\mathrm{d}p_0}{\mathrm{d}t} + \nabla \cdot (\lambda \nabla T), \tag{3}$$

$$\frac{\partial \rho Y_\mathrm{v}}{\partial t} + \nabla \cdot (\rho \boldsymbol{u} Y_\mathrm{v}) = \nabla \cdot (\rho \mathscr{D} \nabla Y_\mathrm{v}). \tag{4}$$

According to standard notation, ρ is the density and $\boldsymbol{u} = (u, v, w)$ is the velocity vector. Also, T stands for the temperature while Y_v denotes the concentration of water vapor in the gaseous domain. p_0 is the thermodynamic pressure and corresponds to the first-order term of the low-Mach number expansion of the pressure. Since we consider an open domain in this study, p_0 is constant and equal to its value at the open boundary which is the atmospheric pressure. Further p' represents the piezometric pressure [2] which reads,

$$p' = p + \rho g y, \tag{5}$$

with y being the spatial coordinate in the vertical direction (opposite to gravity), g the gravitational acceleration and p the sum of the dynamic and bulk viscous pressures [42].

Further, $\boldsymbol{S}$ is twice the deviatoric part of the strain-rate tensor, $\boldsymbol{S} = (\nabla \boldsymbol{u} + (\nabla \boldsymbol{u})^\top) - \frac{2}{3}(\nabla \cdot \boldsymbol{u})\boldsymbol{I}$, with $\boldsymbol{I}$ being the identity matrix. Also μ is the dynamic viscosity, λ the thermal conductivity, and $\mathscr{D}$ is the molecular diffusivity of water vapor in air. With regard to the energy equation (3) since p_0 constant, then the specific enthalpy h_s is a function of the temperature only; in particular, $dh_s = c_p dT$, where c_p refers to the specific heat capacity under constant pressure.

The above system is valid for both phases. The flow quantities are cast in a unified manner via the indicator function $I(\boldsymbol{x}, t)$ which is equal to unity in the gas and zero in the water. For example, the density ρ is written as,

$$\rho = \rho^l(T, p_0) + I(\boldsymbol{x}, t) \left(\rho^g(T, p_0) - \rho^l(T, p_0) \right), \tag{6}$$

where the superscripts l and g refer, respectively, to the water and air-vapor mixture.

The air-vapor mixture is treated as an ideal gas and, therefore,

$$p_0 \;=\; \rho^g \frac{R_u}{M^g} T^g \,. \tag{7}$$

In this equation R_u is the universal gas constant and M^g the molar mass of the gaseous mixture,

$$M^g \;=\; \left(\frac{1-Y_v}{M_a} + \frac{Y_v}{M_v} \right)^{-1} , \tag{8}$$

where M_a and M_v are respectively, the molar mass of dry air and water.

The dynamic viscosity μ^g and thermal conductivity λ^g of the gas are approximated by a Sutherland-type law,

$$\mu^g = \mu_c^g \left(\frac{T^g}{T_c} \right)^{0.7} , \qquad \text{and} \qquad \lambda^g = \lambda_c^g \left(\frac{T^g}{T_c} \right)^{0.7} , \tag{9}$$

with T_c the ambient temperature (prescribed at the open-top boundary) and μ_c^g and λ_c^g the dynamic viscosity and thermal conductivity of ambient air at T_c. The specific heat capacity of the gas c_p^g is assumed to be constant and equal to that of ambient air. This approximation is deemed satisfactory, in view of the temperature range in the problem under study. Additionally, the molecular diffusivity in the air-vapor mixture is computed as follows [35],

$$\mathscr{D} \;=\; 1.87 \times 10^{-10} \; \frac{{T^g}^{2.072}}{p_0} \,, \tag{10}$$

with p_0 expressed in bar. In our case, $p_0 = 1$ bar.

The liquid water is assumed to obey an isobaric equation of state, *i.e.* its density is function of the temperature only. Herein it is approximated by a fourth-order polynomial fit of the tabulated data of [25],

$$\rho^l \;=\; c_4 {T^l}^4 + c_3 {T^l}^3 + c_2 {T^l}^2 + c_1 T^l + c_0 \,, \tag{11}$$

with c_0 - c_4 being the polynomial coefficients. Similarly, the heat capacity, dynamic viscosity and thermal conductivity of the water are also approximated by fourth-order polynomial fits of the data of [25]. The values of the coefficients in these fits are provided in [18, 34].

It is convenient to introduce reference values for purposes of non-dimensionalization of the numerical results and for the introduction of the relevant dimensionless groups. The atmospheric pressure p_0 is the reference pressure. Since convection is developed in both columns, we use two reference temperatures. The one in the water column is the average of the bottom temperature and the initial temperature of the free surface. Similarly, the reference temperature in the gas is the average between the ambient atmospheric temperature and the initial one of the free surface. The differences between the bottom-top temperatures at the two columns are denoted by ΔT^l for the water and ΔT^g for the air. H is the total height of the cuboid, while h_0 is the initial height of the water column and serves as the reference length. The free-fall velocity in the water column $u_{\text{ff}} = \sqrt{g h_0 \beta^l \Delta T^l}$ is the reference velocity, where β^l

is the thermal expansion coefficient of water at its reference temperature. Similarly, β^g is the thermal expansion coefficient of air at the reference temperature in air. Finally, the free-fall time in the water column, $t_{\rm ff} = \frac{h_0}{u_{\rm ff}}$, serves as the reference time.

Following [11], since we have two separated fluid columns, we introduce two sets of dimensionless numbers, one for each column. For the water column, the Prandtl and Rayleigh numbers are given by,

$$Pr^l = \frac{\nu^l}{\alpha^l}, \qquad Ra^l = \frac{g\beta^l \Delta T^l h_0^3}{\nu^l \alpha^l}, \tag{12}$$

with ν^l the kinematic viscosity and $\alpha^l = \frac{\lambda^l}{\rho^l c_p^l}$ the thermal diffusivity of the liquid water at the reference state. Similarly, the Prandtl, Rayleigh numbers and Lewis numbers for the gas column are defined as,

$$Pr^g = \frac{\nu^g}{\alpha^g}, \qquad Ra^g = \frac{g\beta^g \Delta T^g (H-h_0)^3}{\nu^g \alpha^g}, \qquad Le^g = \frac{\alpha^g}{\mathscr{D}}, \tag{13}$$

with the kinematic viscosity ν^g and thermal diffusivity $\alpha^g = \frac{\lambda^g}{\rho^g c_p^g}$ of air being evaluated at the reference thermodynamic state.

2.2. Jump relations

The above system of balance laws (1)–(4), is closed with appropriate jump conditions of the flow variables at the free surface. The jump of the generic variable ϕ from the water side to the gas side is denoted by $[\phi] = \phi^l - \phi^g$. In our study, the free surface of the water, F, is approximated as a flat horizontal surface. For the physical and geometrical parameters considered herein, this hypothesis has been validated on the basis of the work of Liu et al. [28] on two-layer thermally driven turbulence. Below we list the jump relations across F. Details on their derivation can be found in [52] and in [10, 23, 59].

- Temperature,

$$[T] = 0, \qquad \left[\lambda \frac{\partial T}{\partial y}\right] = -\dot{m}'' L^{lg}, \tag{14}$$

  with $\dot{m}''$ the local evaporative mass flux and L^{lg} the latent heat of evaporation of water.

- Density,

$$[\rho] = \rho^l(T_F, p_0) - \rho^g(T_F, p_0), \tag{15}$$

  with T_F the local temperature at the free surface.

- Vapor mass fraction,

$$[Y_{\rm v}] = 1 - Y_{v,F}, \qquad \text{and} \quad -\rho^g \mathscr{D} \frac{\partial Y_v}{\partial y} = \dot{m}''(1 - Y_{v,F}) \quad \text{at } F, \tag{16}$$

  with $Y_{v,F}$ the mass fraction of water vapor at the free surface. Liquid water is assumed to be at equilibrium with its vapor. Therefore, the partial pressure of water vapor at the interface is equal

to the saturation pressure. The vapor concentration at the interface is $Y_{v,F}$ and is then computed on the basis of the vapor saturation and thermodynamic pressures.

- Normal velocity component,

$$[v] = \dot{m}''\,(\frac{1}{\rho^l} - \frac{1}{\rho^g}), \qquad \text{and} \quad v^l = 0, \quad v^g = -\dot{m}''\left(\frac{1}{\rho^l} - \frac{1}{\rho^g}\right) \quad \text{at } F. \tag{17}$$

- Tangential velocity components,

$$[u] = [w] = 0, \qquad \left[\mu\frac{\partial u}{\partial y}\right] = \left[\mu\frac{\partial w}{\partial y}\right] = 0. \tag{18}$$

- Piezometric pressure,

$$[p'] = \dot{m}''^2\left(\frac{1}{\rho^g} - \frac{1}{\rho^l}\right) + [\rho]\,g\,h + \left[2\mu\frac{\partial v}{\partial y} - \frac{2}{3}\mu\nabla\cdot\boldsymbol{u}\right], \tag{19}$$

where h is the distance between the free surface and the bottom wall, *i.e.* the instantaneous height of the water column. It is noted that the evaporative flux $\dot{m}''$ does not appear in the jump relation of the shear stresses in (18) but always appears in the jump relation of the piezometric pressure (19). In other words, at the interface, the shear stresses are continuous whereas the piezometric pressure is discontinuous.

The system of balance laws (1)–(4), coupled with the above jump relations, is integrated numerically with the time-accurate numerical scheme for low-Mach number flows of liquid-gas systems [10]. This algorithm is an extension of the low-Mach number solver [26] for single-phase flows and incorporates a numerical procedure for the tracking of the free surface that is based on the ghost-fluid method. Details of the flow solver and the interface-tracking algorithm are provided in [10], along with a series of validation tests. Since its design and development, the algorithm has been successfully applied in DNS of turbulent natural convection in liquid-gas systems [11].

3. Outline of POD

As mentioned above, POD was first employed in fluid mechanics by Lumley [31, 32] for the study of coherent structures in turbulent flows. In statistics, this procedure is referred to as principal-components analysis and in signal processing as Karhunen-Loève decomposition [24, 30]. The underlying principle of POD is to consider an unsteady flow as a juxtaposition of several structures (or modes) whose intensities vary in time. The objective is then to suitably decompose the flow in order to obtain those modes which form a set of coherent structures. This decomposition produces modes that are orthogonal, *i.e.* uncorrelated with one another, and optimal in the sense that the first k modes contain as much energy of the flow as any other decomposition. A review of the application of POD in turbulent flows can be

found in [6]. Also, a tutorial on POD with emphasis on applications in fluid dynamics is presented in [62]. Further, an overview of modal decomposition methods (including POD) for various flow problems is provided in [58]. Below we provide a brief account of the elements of this technique.

3.0.1. Definitions

We consider a three-dimensional flow domain Ω and its discretization via a computational mesh that consists of a total number of M cells. Let $\boldsymbol{x} = (x, y, z)$ denotes the position vector of any point in the flow domain. The position vector of the center of a computational cell m is denoted by $\boldsymbol{x}_m$, $m = 1, \ldots, M$. First we introduce the concatenated vector $\boldsymbol{q}$ that consists of the five flow variables of interest, $\boldsymbol{q} = (q^1, q^2, q^3, q^4, q^5) = (u, v, w, T, Y_\mathrm{v})$. Values of all the components of $\boldsymbol{q}$ are provided at the cell centers of the computational mesh and at all time instances, t^n, of the computation. The time average of $\boldsymbol{q}$ is denoted by $\langle \boldsymbol{q} \rangle_t$. Its fluctuation, $\boldsymbol{q}' = (u', v', w', T', Y'_\mathrm{v})$, is given by $\boldsymbol{q}' = \boldsymbol{q} - \langle \boldsymbol{q} \rangle_t$. Further, the so-called POD energy of the fluctuations, E_{POD}, over Ω is defined as the integral of the time average of $\boldsymbol{q}' \cdot \boldsymbol{q}'$,

$$E_{POD} \;=\; \int_\Omega \langle \boldsymbol{q}' \cdot \boldsymbol{q}' \rangle_t \, d\boldsymbol{x} \;=\; \int_\Omega \left(\langle \boldsymbol{u}' \cdot \boldsymbol{u}' \rangle_t + \langle T' \cdot T' \rangle_t + \langle Y'_\mathrm{v} \cdot Y'_\mathrm{v} \rangle_t \right) d\boldsymbol{x} \,. \tag{20}$$

For the purposes of POD, we consider a sequence of instantaneous values of $\boldsymbol{q}(\boldsymbol{x}, t^n)$ at N time instances (snapshots), $n = 1, \ldots, N$. These instantaneous values are referred to as snapshots and are taken over a constant time increment. In other words, the time difference between two successive snapshots is constant.

The objective is to decompose each fluctuation, $\boldsymbol{q}'(\boldsymbol{x}, t^n)$, into a sum of N modes $\boldsymbol{\Phi}_k(\boldsymbol{x})$,

$$\boldsymbol{q}'(\boldsymbol{x}, t^n) = \sum_{k=1}^{N} \sqrt{\lambda_k} \mathscr{A}_k(t^n) \, \boldsymbol{\Phi}_k(\boldsymbol{x}) \,, \qquad n = 1, \ldots, N \,. \tag{21}$$

In the above equation, λ_k is the k-th eigenvalue of the correlation matrix $\boldsymbol{R}_{n\tilde{n}}$, $k = 1, \ldots, N$, which represents the POD energy of each mode,

$$\boldsymbol{R}_{n\tilde{n}} \;=\; \frac{1}{N} \int_\Omega \boldsymbol{q}'(\boldsymbol{x}, t^n) \cdot \boldsymbol{q}'(\boldsymbol{x}, t^{\tilde{n}}) \, dV \,. \tag{22}$$

Also in (21) $\boldsymbol{\Phi}_k(\boldsymbol{x})$ is the k-th normalized spatial mode while $\mathscr{A}_k$ is the k-th normalized temporal mode, $k = 1, \ldots, N$. It is noted that in equation (21), all the modes are ordered in terms of the values of the eigenvalues λ_k, from the highest to the lowest one.

The spatial modes before normalization, $\boldsymbol{\phi}_k(\boldsymbol{x}) = (\phi_k^1, \phi_k^2, \phi_k^3, \phi_k^4, \phi_k^5)$, are obtained as solutions of the following eigenproblems,

$$\int_\Omega \sum_{i=1}^{5} \langle q'^j(\boldsymbol{x}, t^n) q'^i(\tilde{\boldsymbol{x}}, t^n) \rangle_t \, \phi_k^i(\boldsymbol{x}) \, d\tilde{\boldsymbol{x}} \;=\; \lambda_k \phi_k^j(\boldsymbol{x}) \,, \qquad k = 1, \ldots, N \,. \tag{23}$$

For numerical purposes, one eigenproblem has to be solved for each component of $\boldsymbol{\phi}_k$ and for each cell center of the computational mesh. However, since the number of computational cells is very high,

and in particular much higher than the number of snapshots, solving these eigenproblems would be overly expensive from the computational point of view. This difficulty is circumvented by employing the method of snapshots introduced by Sirovich [51]. According to it, one assumes that the spatial modes can be written as a linear combination of N instantaneous flow fields (snapshots). This allows to replace (23) by the following simpler eigenproblems,

$$\boldsymbol{R}_{n\tilde{n}}\boldsymbol{A}_k = \lambda_k \boldsymbol{A}_k\,, \qquad k = 1,\ldots,N\,, \tag{24}$$

with the eigenvectors $\boldsymbol{A}_k$ being the temporal modes before normalization. Finally, once these eigenproblems are solved, the spatial modes $\boldsymbol{\phi}_k$ are computed from the temporal modes via the relation,

$$\boldsymbol{\phi}_k(\boldsymbol{x}) = \sum_{n=1}^{N} \boldsymbol{A}_k(t^n)\,\boldsymbol{q}'(\boldsymbol{x},t^n)\,, \qquad k = 1,\ldots,N\,. \tag{25}$$

Below we outline the procedure for the computation of the correlation matrix, the temporal modes and the spatial modes.

3.0.2. Computation of the correlation matrix and the normalized modes

In order to proceed with the decomposition of $\boldsymbol{q}'(\boldsymbol{x},t)$ and the computation of the correlation matrix, we construct the matrix $\boldsymbol{Q}$ which contains the arrays $\boldsymbol{q}'(\boldsymbol{x},t^n)$ at all time instances. In other words, $\boldsymbol{Q}$ is defined as,

$$\boldsymbol{Q} = \begin{pmatrix}
u'(\boldsymbol{x}_1,t^1) & \cdots & u'(\boldsymbol{x}_1,t^N) \\
\vdots & \ddots & \vdots \\
u'(\boldsymbol{x}_M,t^1) & \cdots & u'(\boldsymbol{x}_M,t^N) \\
v'(\boldsymbol{x}_1,t^1) & \cdots & v'(\boldsymbol{x}_1,t^N) \\
\vdots & \ddots & \vdots \\
v'(\boldsymbol{x}_M,t^1) & \cdots & v'(\boldsymbol{x}_M,t^N) \\
w'(\boldsymbol{x}_1,t^1) & \cdots & w'(\boldsymbol{x}_1,t^N) \\
\vdots & \ddots & \vdots \\
w'(\boldsymbol{x}_M,t^1) & \cdots & w'(\boldsymbol{x}_M,t^N) \\
T'(\boldsymbol{x}_1,t^1) & \cdots & T'(\boldsymbol{x}_1,t^N) \\
\vdots & \ddots & \vdots \\
T'(\boldsymbol{x}_M,t^1) & \cdots & T'(\boldsymbol{x}_M,t^N) \\
Y'_{\mathrm{v}}(\boldsymbol{x}_1,t^1) & \cdots & Y'_{\mathrm{v}}(\boldsymbol{x}_1,t^N) \\
\vdots & \ddots & \vdots \\
Y'_{\mathrm{v}}(\boldsymbol{x}_M,t^1) & \cdots & Y'_{\mathrm{v}}(\boldsymbol{x}_M,t^N)
\end{pmatrix}. \tag{26}$$

Next we introduce the weight matrix $\mathscr{W}$. This is the $5M \times 5M$ diagonal matrix that contains the

square roots of the cell volumes V_m, $m = 1,\ldots,5M$, [53],

$$\mathscr{W} = \begin{pmatrix} \sqrt{V_1} & \cdots & 0 & 0 & \cdots & 0 & \cdots \\ \vdots & \ddots & \vdots & 0 & \cdots & 0 & \cdots \\ 0 & \cdots & \sqrt{V_M} & 0 & \cdots & 0 & \cdots \\ 0 & \cdots & 0 & \sqrt{V_1} & \cdots & 0 & \cdots \\ \vdots & \cdots & \vdots & 0 & \ddots & 0 & \cdots \\ 0 & \cdots & 0 & 0 & \cdots & \sqrt{V_M} & \cdots \\ 0 & \cdots & 0 & 0 & \cdots & 0 & \ddots \end{pmatrix}. \tag{27}$$

We can then compute the product between $\mathscr{W}$ and $\boldsymbol{Q}$, denoted by $\mathscr{Q}$,

$$\mathscr{Q} = \mathscr{W}\,\boldsymbol{Q}. \tag{28}$$

The correlation matrix $\boldsymbol{R}_{n\tilde{n}}$ (22) can then be approximated as follows,

$$\boldsymbol{R}_{n\tilde{n}} \approx \frac{1}{N}\mathscr{D}^T\mathscr{D}. \tag{29}$$

To obtain the temporal modes $\boldsymbol{A}_k$, we compute the eigenvalues λ_k, $k = 1,\ldots,N$, of the correlation matrix $\boldsymbol{R}_{n\tilde{n}}$ and order them from the largest ($k = 1$) to the smallest value ($k = N$). Subsequently, we solve the eigenproblem (24) for each mode k to obtain the corresponding unit vector $\boldsymbol{A}_k$. Next, the spatial modes $\boldsymbol{\phi}_k$ are computed from the equation (25). Finally, the normalized spatial and temporal modes are obtained from

$$\boldsymbol{\Phi}_k = \frac{1}{\sqrt{\lambda_k N}}\boldsymbol{\phi}_k, \qquad k = 1,\ldots,N, \tag{30}$$

and

$$\mathscr{A}_k = \sqrt{N}\boldsymbol{A}_k, \qquad k = 1,\ldots,N, \tag{31}$$

respectively.

3.1. On the definition of the POD energy

With regard to the POD analysis presented herein, it is worth noting that the distribution of the energy of the fluctuations E_{POD}, depends on the way that this energy is defined. According to (20), E_{POD} is defined as the sum of the inner products of the velocity, temperature and vapor mass fraction fluctuations. If one had considered the velocity fluctuations only, then E_{POD} would have been equal to the turbulent kinetic energy of the flow $\boldsymbol{u}'.\boldsymbol{u}'$. In that case, the eigenproblem (24) would have led to different energy distribution [22, 43].

In fact, the authors of [4, 33, 44, 45] performed POD analysis of RBC based on the velocities and temperature. In those works, a mixed formulation of the POD energy was employed by introducing a scaled temperature (with the ratio of the inner products of the velocity and temperature being the

scaling factor) and by equating the turbulent kinetic energy with the energy of the thermal fluctuations. It was then observed that the definition of E_{POD} affects not only the POD energy distributions but also the orderings of the spatial and temporal modes. Nonetheless, the definition of E_{POD} does not affect the spatial modes themselves. For this reason, in our study, we have not set the turbulent kinetic energy equal to the energy of the thermal fluctuations. Moreover, such a choice would be cumbersome to implement since our snapshots involve flow quantities from both phases. In any case, our simulations predicted that, in dimensionless terms, the turbulent kinetic energy $\boldsymbol{u}' \cdot \boldsymbol{u}'$ is much higher than the energies of the fluctuations of the temperature and vapor mass fraction, $(T' \cdot T')$ and $Y'_{\mathrm{v}} \cdot Y'_{\mathrm{v}}$, respectively. Consequently, the spatial modes are ordered in terms of the intensity of their turbulent kinetic energy.

Another important point is that in the flow under study the ratio between the water and air densities is very large. But since the kinetic energy is proportional to the density of the media of each column, this means that the inner product of the velocity fluctuations $\boldsymbol{u}' \cdot \boldsymbol{u}'$ cannot provide a reliable representation of the turbulent kinetic energy in both columns simultaneously. The complexities that are caused by the large density ratio can be circumvented by two different approaches. The first one is to include the mass density at each cell in the weight matrix of the POD $\mathscr{W}$ [12, 49]. The second one is to apply the decomposition in the water and gas columns separately [37, 38]. In the context of our study, we tested both approaches and observed that in the first approach, the fluid column with the higher turbulent kinetic energy imposes its structure on the other one. This implies that POD in the column with the lower energy is not performed optimally. For this reason we have opted for the second approach and performed POD for the water and gas columns separately.

4. Numerical setup and main features of the flow

Before proceeding with the results of our POD analysis, we outline the numerical setup and discuss the organization of the flow in the two columns.

4.1. Numerical setup

The flow domain is the same as in [11]. More specifically, it is an open-top cuboid with height (in the vertical y direction) $H = 11.5$ cm and width (in the horizontal x and z directions) $W = 4.5$ cm. Its lower part contains liquid water. The initial height of the water column is $h_0 = 2.25$ cm, which is also the initial height of the free surface. The upper part (above the free surface) is occupied by humid air. Accordingly, the initial aspect ratios of the water and gas columns are $\Gamma^l = \frac{W}{h_0} = 2$ and $\Gamma^g = \frac{W}{H-h_0} = 0.5$, respectively. The temperature of the bottom wall is uniform and fixed at $T_h = 315.25$ K. Whereas the open-top boundary is maintained at the temperature of the ambient air above the cuboid $T_c = 298.15$ K. Given these parameters, the (initial) Rayleigh number in the gas column is $Ra^g = 10^6$. Also, the (initial) Rayleigh number in the water column is $Ra^l = 6 \times 10^5$. These values are such that turbulent convection

of moderate intensity is established in both phases. A schematic representation of the computational domain is provided in figure 1.

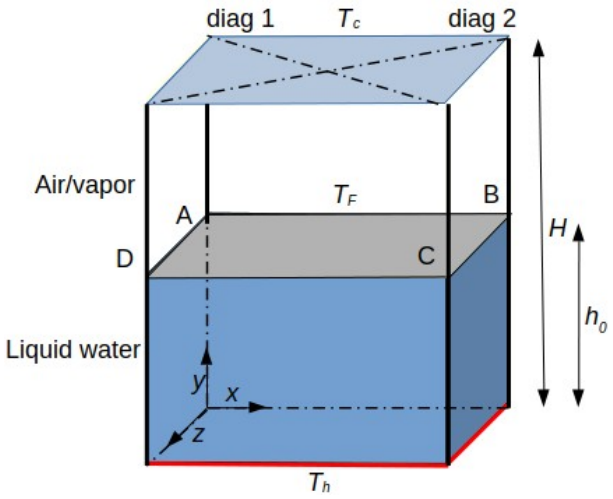

Figure 1: Computational domain and coordinate system. The warm bottom wall is maintained at T_h, while the cooler top boundary is at T_c. The grey plane depicts the initial position of the free surface at h_0. The letters A, B, C and D refer to the points at the corners of the free surface.

With regard to boundary conditions, zero-Neumann data are prescribed for the temperatures and vapor mass fraction at the vertical boundaries. In other words, the side walls are assumed to be adiabatically isolated. As mentioned above, Dirichlet thermal conditions are prescribed at the bottom and top boundaries: the temperatures therein are maintained at T_h and T_c respectively. Similarly, a Dirichlet condition is prescribed for the vapor mass fraction at the top boundary, $Y_v^{amb} = 0.00742$ which corresponds to an ambient relative humidity $RH = 40\%$. Whereas zero-slip kinematics conditions are applied at the bottom and side walls. Concerning the open-top boundary, a convective kinematic condition [16] is used in order to avoid spurious reflections of any flow structures exiting the domain. For details on the implementation of the convective kinematic condition, the reader is referred to [11].

As initial condition, we use an instantaneous flow profile that was obtained from the DNS of [11] once the flow becomes fully developed and all transient effects have decayed. For this reason, the free-surface temperature used to compute t_{ff} and u_{ff} is $T_F = 313.5$ K according to the value reported in [11].

The computational mesh used in the DNS is the same as the one in [11]. To generate the mesh, we have followed the same procedure as in [19, 20] which is based on the grid-resolution criteria of [17, 50, 57] for DNS of turbulent natural convection. The first criterion relates to the resolution of the near-boundary regions and the second one to the resolution in the bulk of the domain, *i.e.* away from boundaries. The mesh resolution are $N_x = N_z = 80$ cells in the x and z directions and $N_y = 240$ cells in the y direction. Details on the mesh generation are available in [11].

4.2. Main features of the flow

The properties of the problem under study have been discussed in [11] and therefore herein we discuss only the basic main features of the flow. With regard to notation, the time average of a generic quantity ϕ is denoted by $\langle\phi\rangle_t$, the instantaneous area average in the xz plane by $\langle\phi\rangle_{xz}$, and the combined volume and time average by $\langle\phi\rangle_{xyz,t}$.

In figure 2 we have plotted the evolution of the area-averaged evaporative flux, $\dot{m}''$. According to it, the evaporative flux is stabilized at approximately, $\langle\dot{m}''\rangle_{xz} = 0.15$ g/(m^{2}s), see also relevant discussion in [11]. It can also be observed that $\langle\dot{m}''\rangle_{xz}$ is subject to low-amplitude high-frequency oscillations, presumably due to turbulence at the two sides of the interface. In the same figure we have also plotted the evolution of the height of the water column h. Since the evaporative flux varies little with time, then the rate of decrease of h is practically constant. Additionally, on the basis of this plot, it can be deduced that the total loss of liquid water during the simulation (400 t_{ff}) is equal to 0.5% of the initial mass of liquid water.

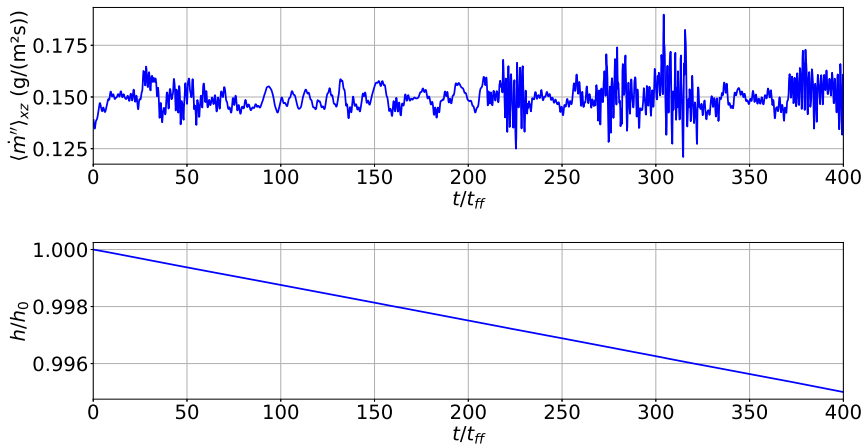

Figure 2: Evolution of the evaporative flux (top) and the height of the water column (bottom).

Figure 3 depicts the evolution of the area-averaged temperature at the free surface $\langle T_F\rangle_{xz}$. According to it, the temperature of the free surface is stabilized at approximately, $\langle T_F\rangle_{xz} = 313.9$ K; see also relevant discussion in [11]. Similarly to the evaporative flux, $\langle T_F\rangle_{xz}$ is also subjected to high-frequency oscillations. The amplitude of these oscillations is also quite low, 0.1 K or less, and is also attributed to the turbulence of the flow. It is noted that the fluctuations of $\langle T_F\rangle_{xz}$ are too small to have an impact on the Rayleigh numbers Ra^l and Ra^g. In particular, the computed fluctuations of $\langle T_F\rangle_{xz}$ result in a 0.65% variation of Ra^g and a 6% variation of Ra^l. Such variations are too small to exert a noticeable effect on the flow statistics in the two phases. It is also worth adding that, in terms of sensibility analysis, in our study [11] we performed simulations at different values of Ra^g in the range of $10^4 - 10^6$. According to our analysis, in that range, the evaporative flux and free-surface temperature are only slightly affected by

the turbulence intensity in the gas column.

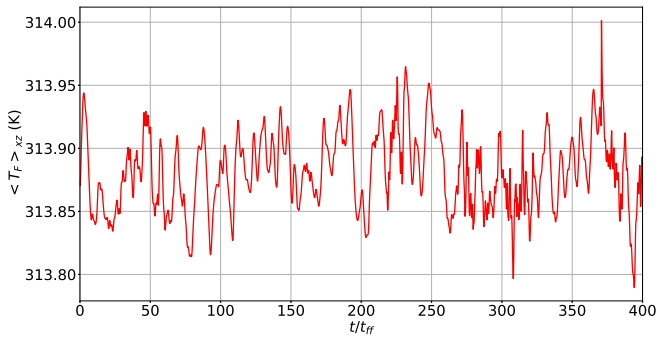

Figure 3: Evolution of the temperature of the free surface.

In figure 4 we present time-averaged streamlines colored by the time-averaged temperature. These plots are obtained by averaging 2000 snapshots (instantaneous profiles) over a time period of 400 t_{ff}; in other words, the sampling interval is 0.2 t_{ff}. These are the same snapshots that were used for our POD analysis. The results shown herein are very close to the corresponding time-averaged results in [11] which were obtained at a much higher sampling rate and are not shown herein for the purposes of the economy of space. This in turn is an indication that the selected averaging period and sampling interval are adequate for the purposes of POD.

Further, it is interesting to observe that in figure 4, the impingement points of the large-scale circulations of the two columns on the free surface are close to one another. These impingement points are near corner D close to the diagonal D-B (diagonal 2). As discussed in [11], this is due to the continuity of the shear stresses across the free surface and implies that the flow structures in the two columns interact with one another.

In figure 5 we provide color plots of the time-averaged temperature, superimposed with the time-averaged vector plots, at the two diagonal planes. These plots are obtained from the same 2000 snapshots mentioned above. Concerning the water column, figure 5b shows that the large-scale circulation of the flow consists of a main roll in the diagonal plane 2 (with an axis in the diagonal plane 1), and of a corner structure. Hereafter, when referring to the water column, we will use the expressions *large-scale circulation* and *main convective roll* interchangeably.

The extent of the main roll coincides with the impingement point. The heat is essentially transported vertically in this impingement region. Figure 5b also shows that the impingement region coincides with a strong downward motion of cold fluid in the gas, while at the other side (corner B), warm fluid is transported upwards, thus forming an outer large-scale circulation spanning the entire height of the gas column. The absence of such motion in 5a shows that the large-scale circulation is aligned with the diagonal plane 2. In the gas column, the flow is organized into large-scale circulation consisting of two

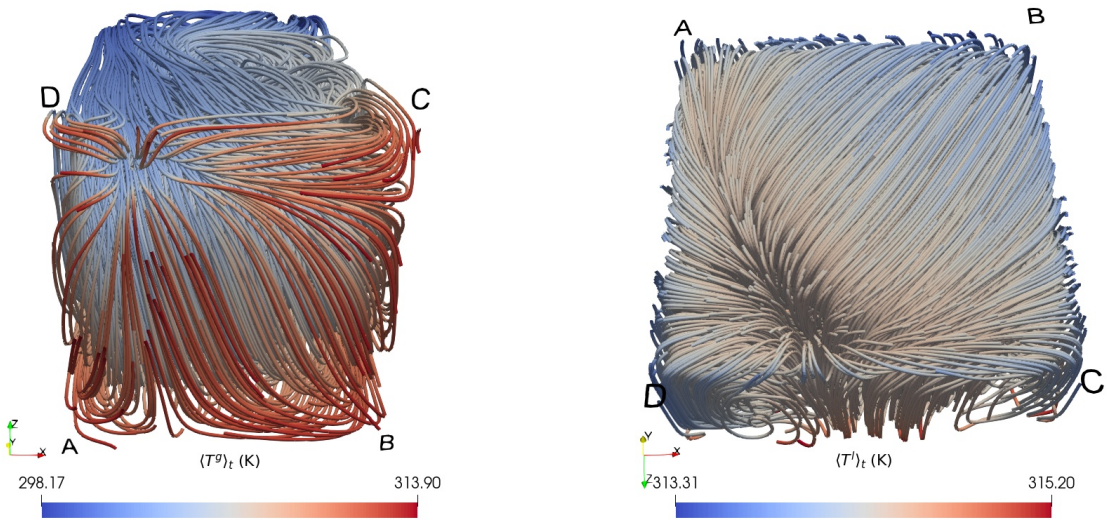

(a) gas column, bottom view. **(b)** water column, top view.

Figure 4: Time-averaged streamlines in both domains colored by the time-averaged temperature. The profiles are obtained by averaging 2000 snapshots over 400 t_{ff}. a) gas column, bottom view. b) water column, top view. The letters A, B, C and D refer to the four corners of the computational domain.

main rolls superposed on top of each other and with axes orthogonal to each other. The bottom roll is aligned in the x axis, while the top one in the z axis. The rolls twist into each other along the diagonal plane 1 (A-C), with a strong shearing motion at mid-height above corner A.

Another interesting prediction of our DNS is that reorientation events of the large-scale circulation in the gas are rare. This can be attributed to the low aspect ratio of the gas column which is known to stabilize the flow structures [1]. Furthermore, reorientation events are rare in the water too. One plausible explanation for this is that in the water such events are inhibited by the convective rolls in the gas.

With regard to the temperature fluctuations, the relative values of the temperature rms in the two phases have been computed with respect to the bottom-top temperature difference of each phase in [11]. It is observed that the relative amplitudes of the temperature rms are quite close to each other with a deviation of 20% of the time-averaged temperature of the respective phase.

An important feature of the flow under study is the effect of evaporation on the convective structures in the two phases. With regard to this effect, we remark that evaporation under the conditions considered herein is a slow process. In particular, the time scale associated to it is much longer than the time scales of turbulent motions. As such, evaporation is not expected to have a direct short-term effect on the flow dynamics. This can be corroborated by the fact that the normal velocity of the gas just above the free surface is three orders of magnitude lower than the velocity in the bulk of the gas. Accordingly, evaporation has only a long-term direct effect, which is the decrease of the size of the water column and the increase of the size of the gas column. Therefore, over long periods of time the turbulence intensity will decrease in the water and increase in the gas.

However, evaporation has an important indirect effect on the emerging turbulent structures in the

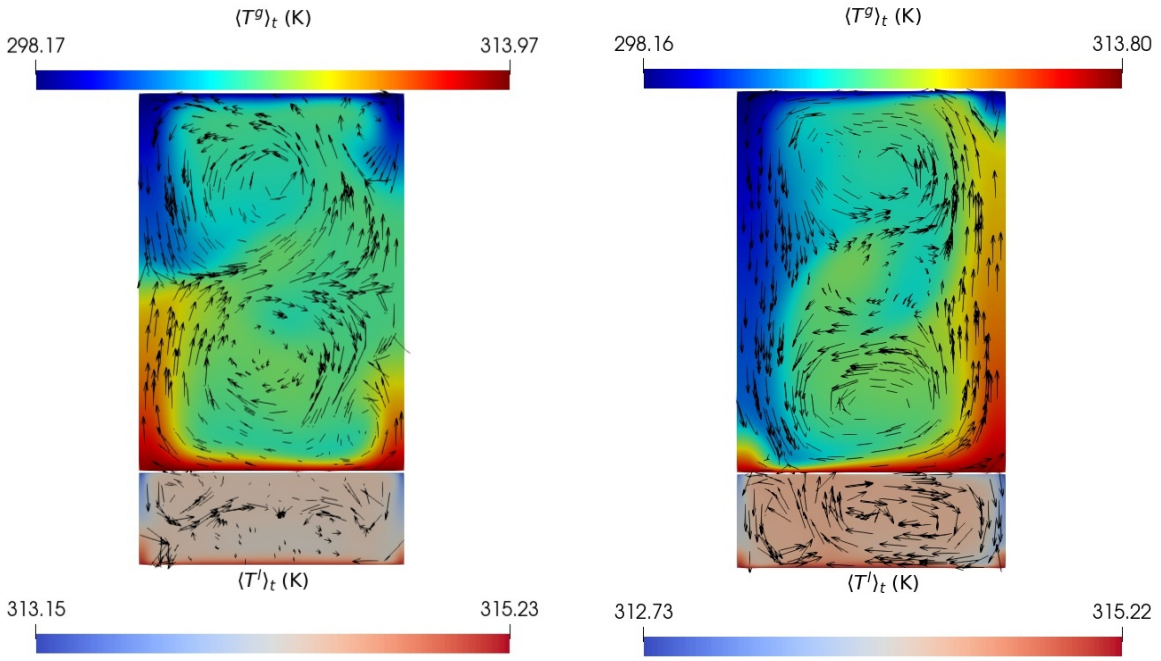

(a) diagonal plane 1. **(b)** diagonal plane 2.

Figure 5: Color plots of time-averaged temperature and superimposed time-averaged vector plots of the velocity. (a) diagonal plane 1 (A-C), (b) diagonal plane 2 (D-B). Since the interface descends, the layers of cells in which the interface was located have been excluded from time averaging and are thus removed from the plots. For visibility purposes, we have used different color maps for each phase.

gas. More specifically, due to evaporation, the gas right above the free surface is at saturation conditions; *i.e.* the vapor concentration therein is kept at the saturation value. This creates a top-bottom difference in vapor concentration which induces convection motions. Their intensity is measured in terms of the concentration Rayleigh number which reads $Ra_c^g = \frac{g\Delta\rho^g(H-h_0)^3}{\mathscr{D}\mu^g}$. For example, for isothermal conditions at temperature $T = 306$ K, the initial concentration Rayleigh number in the gas is $Ra_c^g = 3.4 \times 10^5$. This value is 3 times lower than that of Ra^g but still sufficiently high to establish turbulent natural convection. In other words, in the flow under study, evaporation establishes a difference in vapor concentration which acts as an additional forcing in the gas, besides the forcing due to temperature difference ΔT^g. Accordingly, the observed flow structures in the gas column are the result of the combined effect of thermal and vapor-concentration differences. In summary, due to evaporation, in the gas column we have combined thermal and concentration convection instead of just thermal one.

For the sake of completeness, it is worth mentioning that since our study is based on the low-Mach number equations, the effect of the vapor concentration in the gas density is taken into account in the equation of state of the gas. But if one had chosen to invoke the Boussinesq approximation, then the buoyancy force would consist of two terms, one due to the temperature difference and the other one due to the vapor-concentration difference between the free surface and the open-top boundary [9].

In figure 6, we present the power spectrum S of the signals of the thermal fluctuations at the centers

of each column. In these plots, the signal noise has been suppressed by applying a Gaussian filter. With regard to the water column, in the inertial-convective subrange the spectrum drops following a power law with a slope equal to -5/3, as is the case in channel flows [60] and RBC [21, 39]. Then, at frequencies higher than $f \approx 1$ the spectrum decays rapidly.

Interestingly, the spectrum in the gas column has a more complex profile. It exhibits two peaks, one at a low frequency ($f \approx 0.022$) and a sharp one at high frequency ($f \approx 0.7$). Between these peaks, the spectrum has a slope of -5/3, similarly to the spectrum in the water. Beyond the second peak, the spectrum of the thermal fluctuations assumes again a slope of -5/3 until $f \approx 3$, beyond which it falls off rapidly.

On the one hand, in the low-frequency range, the two spectra exhibit the same trends. This suggests that the interaction between the flow structures in the two columns occurs mostly in this range. In other words, the fluctuations in the water could act like a low-frequency excitation of the gas at the free surface and vice versa. Nonetheless, since the water is more dense and viscous than humid air, it is expected that it is mostly the water fluctuations that modulate those in the air rather than the other way around.

Furthermore, at high frequencies, the energetic content of the thermal fluctuations in the gas is considerable, whereas in the water it is very small. This can be attributed to the fact that the characteristic speeds in the air and in the gas are different: the ratio of the high frequency to low frequency ratio (25) matches that of the free-fall velocities in the air and in the water (about 20). Since it is difficult to draw global conclusions from local measurements, we will use POD analysis to investigate these points in detail in the next section.

For the sake of completeness, we have also examined the spectrum of the vapor mass fraction to the temperature spectrum in the gas column. As it turns out, it is very similar to that of the gas temperature and for this reason is not reproduced herein. The close similarity of the two spectra is consistent with the fact that the Lewis number of air is close to unity, $Le^g \approx 0.82$, for the conditions considered in our study.

5. POD analysis

For a global description of the fluctuations, we now turn to POD analysis. As mentioned in the previous section, all variables of interest (velocity components, temperature and vapor mass fraction) are recorded each $0.2\,t_{\mathrm{ff}}$ for a total duration of $400\,t_{\mathrm{ff}}$, which amounts to a total of $N = 2000$ snapshots. Further, all variables are made dimensionless with respect to the reference quantities in the water column. In order to check the appropriateness of the snapshot sampling we have performed two different PODs in each column; one with 2000 snapshots and one with 400 snapshots. For the second POD, the sampling increment was $1\,t_{\mathrm{ff}}$. The two PODs yielded the same temporal and spatial modes. All results presented in this section refer to the normalized spatial and temporal modes of POD.

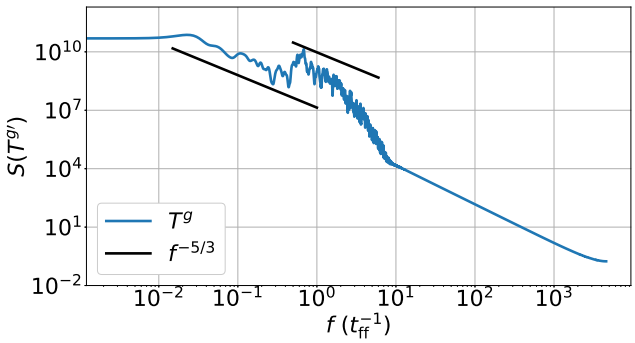

(a) gas column.

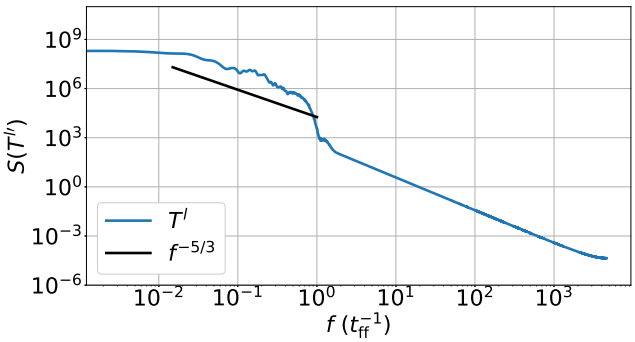

(b) water column.

Figure 6: Power spectra S of the signals of the thermal fluctuations. (a) gas column, (b) water column. The frequency f has been nondimensionalized by t_{ff}^{-1}.

5.1. Spatial modes

We proceed to study the results obtained for the PODs performed in the two columns. The distribution of the POD energy in the spatial modes are shown in figures 7a (for the gas column) and 7b (for the water column). In the same figures, we have also plotted the cumulative POD energies up to the k-th mode, $k = 1, \ldots, N$. According to these figures, the energy distribution in the gas decays much faster than in the water. This may appear counterintuitive, since the gas contains a much wider range of frequencies than the water, while the Rayleigh numbers in the two phases are similar. The fast energy decay in the gas is explained by the fact that the aspect ratio of the gas column is approximately four times lower than that of the water column. While, as mentioned above, it is known that a low aspect ratio tends to stabilize the structures of the flow. This implies that the energies of the dominant modes are higher in a column of low aspect ratio. The distribution of energy in the gas column confirms this fact.

More specifically, in the gas, the first mode accounts for approximately 25% of the total POD energy, while the first 3 modes contain 60% of it. Since the decomposition of the flow is based on the square root of the energy (21), this implies that the first mode represents roughly 50% of the fluctuations of the time-averaged field. Further, we can observe that the decay of the energy of the spatial modes decreases abruptly after the third mode.

On the other hand, the distribution of the POD energy in the water is much smoother. The first mode contains 15% of the total POD energy, which represents roughly 39% of the fluctuations of the time-averaged field. Also, it takes 15 modes to account for 60% of the total POD energy (compared to 3 modes for the gas).

Given the smooth energy distribution in the water column, it would be interesting to examine the streamlines that correspond to the velocity components of the first modes. To this end, in figure 8 we have plotted the streamlines for modes 1–3 and 8, colored with the temperature of the corresponding mode. (We have chosen to present mode 8 instead of mode 4 because the structures of the streamlines that correspond to mode 8 are useful to explain the results obtained by reconstruction of the flow fields that are presented below). According to these plots, warm water corresponds to ascending streamlines, while cold water corresponds to descending ones. This, in turn, shows that the temperature and velocity modes contribute positively to the convective heat flux.

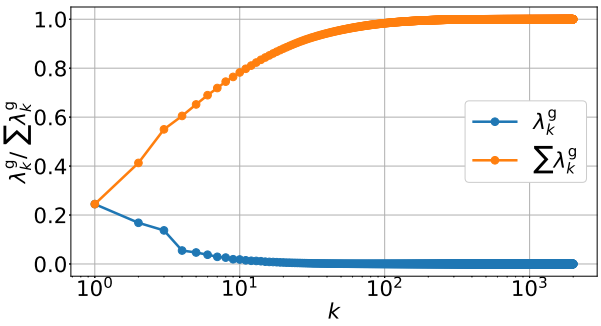

(a) gas column.

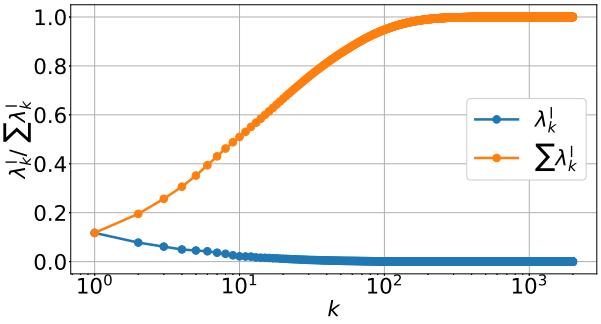

(b) water column

Figure 7: POD energy of the $N = 2000$ modes and cumulative POD energy. a) gas column. b) water column.

In the same figures, we observe that in modes 1–3, the more intense fluctuations are located near the corners A, C and D. In particular, these fluctuations are characterized by relatively large scales taking the form of rolls. With regard to modes 1 and 2, we note that the horizontal alignment of both fluctuating modes is along diagonal 1, i.e orthogonal to the main roll axis. Similarly, according to figure 4 shown

above, the time-averaged streamlines are practically aligned in the second diagonal plane (D-B) and have an impingement point on the free surface close to point D. The effect of the fluctuations due to modes 1 and 2 is therefore to change the strength (and possibly the direction) of the flow streamlines at the interface. Moreover, mode 1 is characterized by a critical point (node-like) close to the mean impingement point and the diagonal, so that it is expected to modulate the size of the convection roll region, but not its orientation. In contrast, mode 2 is characterized by two such connected points, associated with vertical motions of opposite sign on each side of the diagonal plane 2 (B-D). The effect of mode 2 will therefore be to distort streamlines towards the walls and away from the main diagonal.

Further, in figure 8d, we can observe that the fluctuation streamlines of mode 8 are much less ordered and more intermingled than those of modes 1–3. Nonetheless, small structures in the forms of rolls are discernible in corners A and C. The rolls impinge on the free surface at almost right angles.

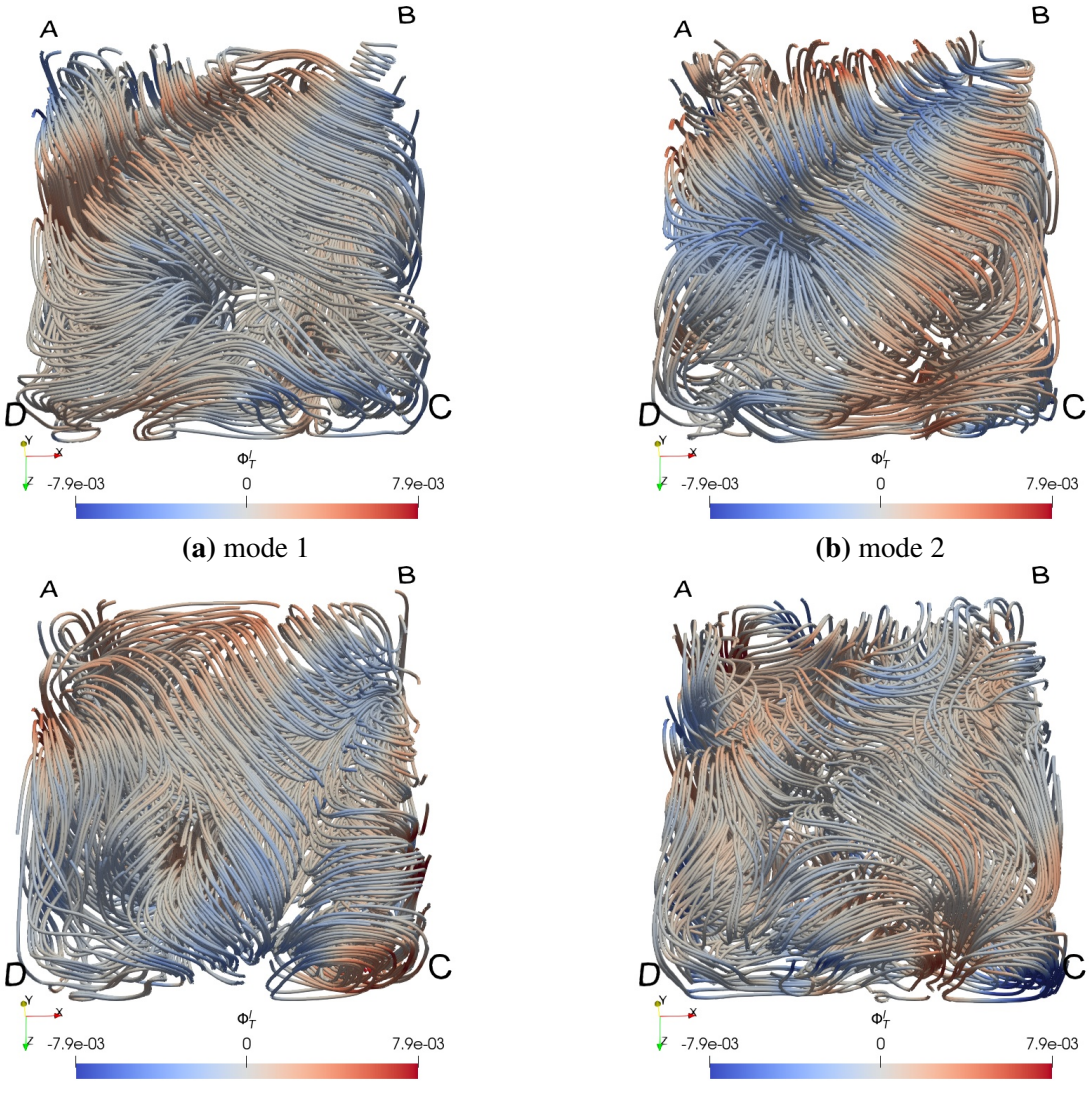

(a) mode 1 **(b)** mode 2

(c) mode 3 **(d)** mode 8

Figure 8: Water column: top view of streamlines corresponding to spatial modes 1–3 and 8, colored by the temperature of the corresponding mode. The color bar is the same for all modes.

For the gas column, in figure 9, we present color plots of the first 2 modes of the thermal fluctuations at the two diagonal planes, superimposed with vector plots of the corresponding velocity modes. A striking fact is that the peaks of the magnitude of the modes (higher positive values and lower negative values) are all located in the bulk of the gas column close to the mid-height plane. We note that since the top and bottom boundary conditions in the gas column are different, the spatial modes are not symmetric.

It is quite cumbersome to educe three-dimensional coherent motions for the full column from the two diagonal planes, as they contain many vortical structures. In diagonal plane 1, a peak is observed at the junction between the two rolls (above A). Mode 1 is characterized by a global pattern that tends to carry warm fluid upwards at C (or cold fluid downwards) through the two-roll pattern. In the other diagonal plane, a strong motion of uniform sign is observed along the cell walls (except at the top above point D), which tends to limit the convective roll. In both planes, the vortical fluctuations tend to accentuate the asymmetry between the strength of the top and bottom rolls. Accordingly, mode 1 involves complex 3D fluctuations of the convective motions of the gas. This issue is discussed further below.

With regard to mode 2, in diagonal plane 1, it is characterized by fluctuations of opposite sign in the top and bottom half of the columns. This means that this mode tends to strengthen or weaken both rolls. In diagonal plane 2, mode 2 is characterized by a strong vortical structure at mid-height, and a weak motion above the impingement point at the interface (near D). Moreover, upon comparison with the plots shown in figure 5, we infer that the 2nd mode follows the time-averaged convective motions. For example, at diagonal plane 2, (figure 9d), we can discern two elongated zones of high-intensity fluctuations (shown in red and blue color, respectively) that are symmetrically located with respect to the center of plane. The locations of these zones coincide with the transition zone between the two large convective rolls that are depicted by the vector plots of the time-averaged velocity in figure 5b. Also, at diagonal plane 1, the hook-shaped zones of high fluctuations at the right edge coincide with similarly shaped zones in the plot of the time-averaged temperature. This suggests that the second-mode fluctuations therein modulate the size and intensity of the corresponding zones of $\langle T^g \rangle_t$. In particular, positive values of the second-mode fluctuations tend to reduce the time-averaged temperature and vice versa.

Further, we have examined the distribution of the first 2 modes of the fluctuations of the vapor concentration. These were very similar to the corresponding modes of the thermal fluctuations, with a correlation coefficient larger than 0.99. This is consistent with the fact that the Lewis number of air is close to unity.

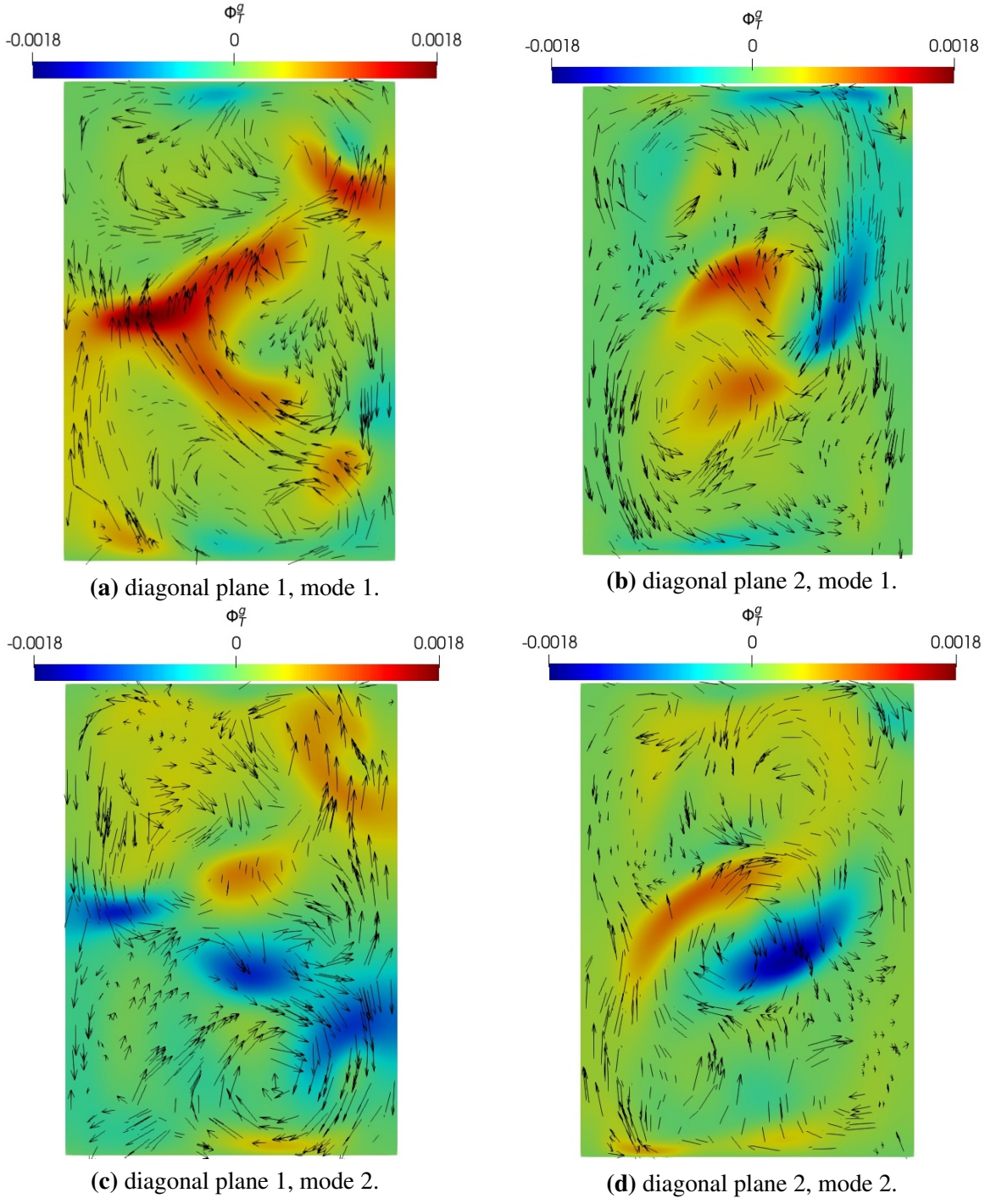

(a) diagonal plane 1, mode 1.

(b) diagonal plane 2, mode 1.

(c) diagonal plane 1, mode 2.

(d) diagonal plane 2, mode 2.

Figure 9: Gas column: color plots of the first 2 spatial modes of the thermal fluctuations, superimposed with vector plots of the corresponding velocity modes. The color bar is the same in all plots. (a) diagonal plane 1 (A-C), mode 1. (b) diagonal plane 2 (D-B), mode 1. (c) diagonal plane 1, mode 2. (d) diagonal plane 2, mode 2.

5.2. Temporal modes

In this section, we analyze the normalized temporal modes obtained from POD in the water and gas columns.

The evolution of the first 4 temporal modes in the gas, $\mathscr{A}_k^g$, $k = 1,\ldots,4$, is provided in figure 10. As observed for the local temperature signal, the amplitudes are apparently chaotic with both high-

frequency and low-frequency components. We can also notice that the first two modes are characterized by infrequent, large, negative values. The spectral intensities of the modes, defined as the square root of their power spectra $\sqrt{S(\mathscr{A}_k^{\mathrm{g}})}$ are represented in figure 11. All modes are characterized by two main ranges of frequencies, one below $f < 0.25$ with a peak around $f_1 \approx 0.022$, and one around $f_2 \approx 0.6$. This is in good agreement with the local measurements described in section 4. The high-frequency energetic content is particularly high for modes 3 and 4. We also observe secondary peaks at intermediate frequencies, between f_1 and f_2.

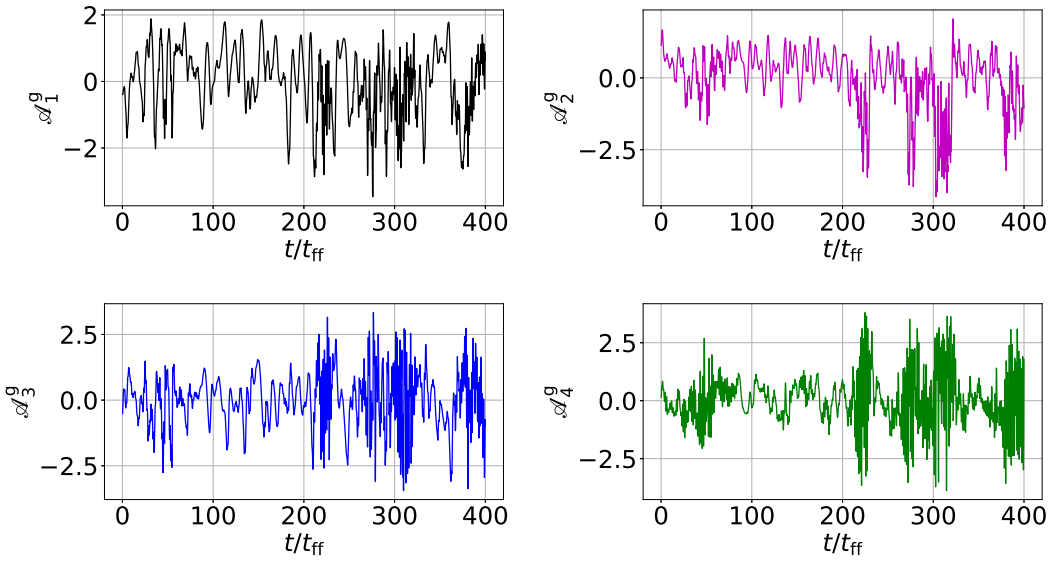

Figure 10: Gas column: evolution of the first 4 temporal modes $\mathscr{A}_k^{\mathrm{g}}$, $k = 1, 2, 3, 4$.

With regard to the water column, the evolution of the first 4 temporal modes, $\mathscr{A}_k^{\mathrm{l}}$, $k = 1, \ldots, 4$, are presented in figure 12. According to this figure, the temporal modes in the water are much smoother than in the gas. More specifically, their signals are characterized by high-amplitude but low-frequency oscillations. Some high-frequency oscillations are also present but their amplitude is quite small.

Further, in figure 13 we have plotted the square roots of the power spectra of the first 4 temporal modes in the water column. All 4 modes are characterized by a single predominant frequency at $f_1 = 0.022$, which coincides with the first dominant frequency of the temporal modes in the gas.

It is now possible to attribute a physical meaning to the low frequencies observed in the global water modes as well as to the high ones observed in the gas mode. According to the reasoning presented in [54], in turbulent natural convection, the frequency of the highest peak of the power spectra corresponds to the time that is necessary for a fluid particle to travel around the perimeter of the large-scale circulation (or main convective roll) of the flow. For computational purposes, the projection of this convective roll on the plane of alignment can be approximated as an ellipse.

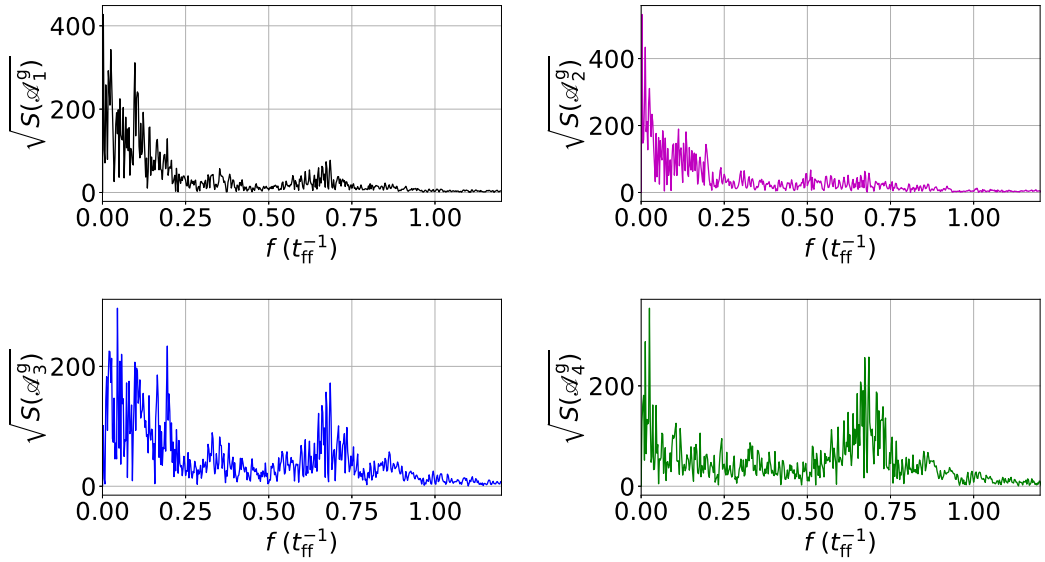

Figure 11: Gas column: square roots of the power spectra of the first 4 temporal modes.

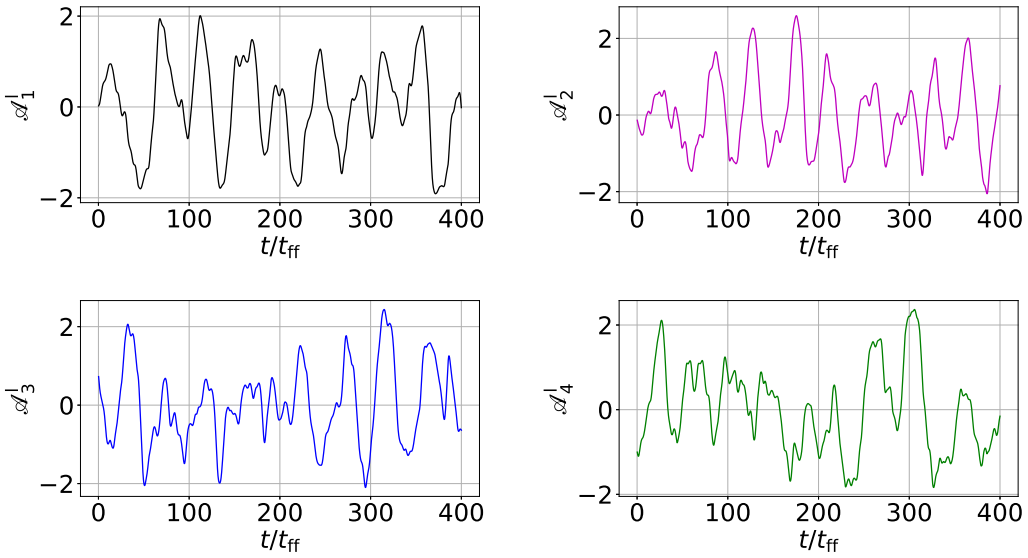

Figure 12: Water column: evolution of the first 4 temporal modes, $\mathscr{A}_k^{\mathrm{l}}$, $k = 1, 2, 3, 4$.

On the basis of this approximation, we infer from figure 5b that the major axis of the main convective roll in the water column is equal to 0.6 of the length of the diagonal of the free surface. Whereas its minor axis is equal to the height of the water column. This allows us to obtain an approximation of the perimeter of the main convective roll. To compute an estimate of the time that it takes for a fluid particle to circumvent the main roll, we use the volume and time average of the velocity norm. By following this procedure, we compute that the frequency associated with the main convective roll is $f^l = 0.022$, which is very close to the dominant frequency f_1 of the power spectra of the first 4 temporal modes.

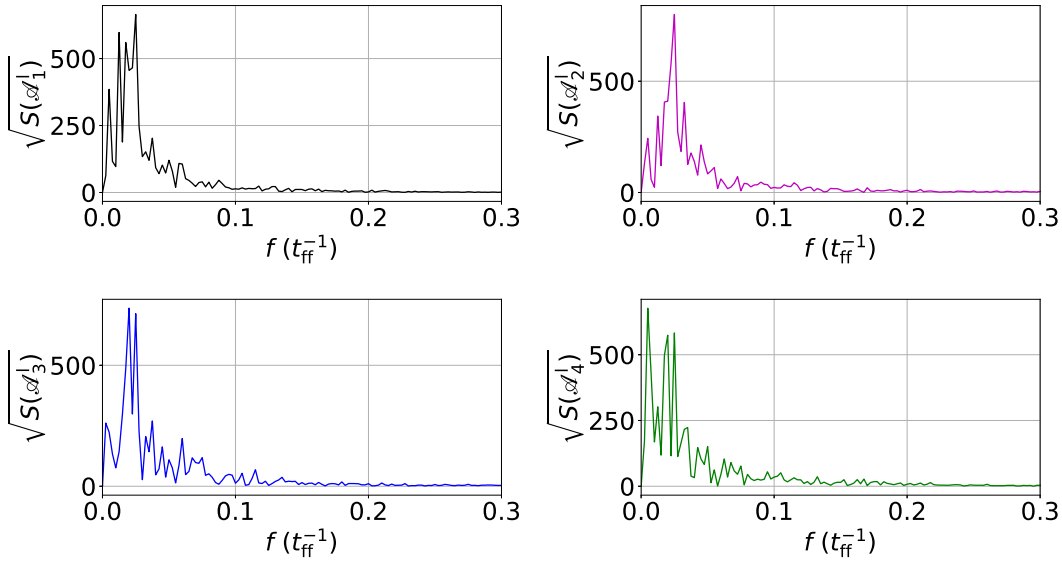

Figure 13: Water column: square roots of the power spectra of the first 4 temporal modes.

The same procedure can be applied in the gas column. More specifically, the major axis of the lower convective roll is equal to 0.6 of the diagonal of the free surface. While its minor axis is equal to 0.3 of the height of the gas column. We then compute that the frequency associated with the dual-roll structure is $f^g = 0.63$. This value is close to the second dominant frequency f_2 of the power spectra of temporal modes 1, 3 and 4. We note that the intermediate frequency around $f = 0.3$ could be attributed to the outer circulation in the gas column. The results for both columns are provided in table 1. They show that the frequencies are consistent with the large-scale circulation in both the water and the gas columns. They also suggest that the low frequency of the gas temporal modes f_1 is associated to modulation of the turbulent motions of air by the main convective roll in the water. In other words, whereas the intermediate and high frequencies are related to the intrinsic flow dynamics in the gas, the low frequency is related to the interaction between the two columns at the free surface and, as such, it affects both the outer roll and the inner dual-roll structure. This point will be elaborated in the next section.

$\langle\lvert\boldsymbol{u}^l\rvert\rangle_{xyz,t}/u_{\mathrm{ff}}$	$\langle\lvert\boldsymbol{u}^g\rvert\rangle_{xyz,t}/u_{\mathrm{ff}}$	P^l/h_0	P^g/h_0	$f^l = \langle\boldsymbol{u}^l\rangle/P^l$	$f^g = \langle\boldsymbol{u}^g\rangle/P^g$
0.097	2.91	4.39	4.63	0.022	0.63

Table 1: Dominant frequencies in the water and air. In this table, P^l and P^g are estimates of the perimeters of the large-scale circulations in the two fluid columns.

5.3. Correlation between temporal modes in the two phases

To investigate if the low-frequency motions in the gas and in the water are connected, we proceed to study the correlation between the first temporal modes in the water and gas. To this end, we have computed the correlation coefficients between these modes. For purposes of comparison, we have also

performed POD of the flow variables of interest on the water side of the free surface. This POD is realized by considering a thin layer of water just below the free surface. This layer corresponds to a small number of horizontal layers of cells. More specifically, the layers that we considered amount for 3% of the height of the water column. Then, it was verified that the spatial hence temporal modes obtained in this manner did not depend on the y variable, thereby confirming that the layer of water that we considered for the POD was sufficiently thin. The decomposition of the flow field obtained in this manner is referred to herein as the POD at the free surface.

First we examine the correlation between the modes of the water and those of the free surface. In table 2 we provide the highest correlation coefficients between the first 10 temporal modes in the water and the 2000 temporal modes at the free surface. According to it each of the first 10 modes in the water (with the exception of mode 8) is well correlated with one of the first 10 modes at the free surface. The correlation coefficients range between 0.42 and 0.8 (for modes 10 and 2 in the water, respectively). The only exception is mode 8 in the water which is weakly correlated to the free-surface modes; its highest correlation coefficient is 0.28. Nonetheless, these results show that overall there is a substantial correlation between the flow dynamics of the water column and those of the interface. This in turn indicates that the water motions can be tracked directly through the free surface.

modes in water	1	2	3	4	5	6	7	8	9	10
modes at the free surface	2	1	3	5	5	6	7	5	10	9
correlation coefficient	0.73	0.8	0.68	0.43	0.58	0.60	0.55	0.28	0.55	0.42

Table 2: Highest correlation coefficients between the first 10 temporal modes in the water and the 2000 temporal modes at the free surface.

We now focus on the correlation between the dominant temporal mode in the water, mode 1, and those at the free surface and in the gas column. The highest correlation coefficients are provided in table 3. According to this table, mode 1 of water is mostly correlated with mode 2 at the free surface. The correlation coefficient is 0.73, which implies strong coupling between these modes.

	mode 2 of the free surface	mode 1 in gas	filtered mode 1 in gas
mode 1 in water	0.731	0.43	0.60

Table 3: Highest correlation coefficients between temporal mode 1 in the water and the 2000 temporal modes in the gas and at the free surface. In the third column, all the frequencies above 0.05 are removed.

With regard to the coupling with the gas, mode 1 in the water is mostly correlated with mode 1 in the gas. The correlation coefficient between them is equal to 0.43, which implies weaker correlation than with the modes at the free surface. Nonetheless, this value (0.43) is still sufficiently high to suggest considerable interaction between the fluctuations in the two columns. At this point, it is worth recalling that the signal of the temporal modes in the gas is rich in low-frequency low-amplitude oscillations.

Motivated by this fact, we have examined the correlation between the low-frequency content of the gas modes with mode 1 of the gas. To this end, we filter out all frequencies higher than 0.05. According to our analysis, mode 1 of the water is strongly correlated to filtered mode 1 of the gas, with a correlation coefficient equal to 0.60. In other words, the interaction between the first modes in the two columns occurs mostly via the low-frequency component of the gas mode.

As a side note, we may add that the maximum correlation between the free surface and the gas involves modes 1 and 5 respectively, with the coefficient being equal to 0.39. This suggests that the dynamics of the turbulent motions in the gas are, at least partially, related to those at the free surface.

The connection between the dominant POD modes in the water and gas is further established by computing their coherence, C^{lg}, the plot of which is shown in figure 14. The coherence is quite high at low frequencies and attains a maximum of 0.6 at $f_1 = 0.022$, which corresponds to the dominant frequencies of the temporal modes and is associated to the main convective roll in the water. On the other hand, the coherence at medium and high frequencies is very low. These findings confirm the connection in the low-frequency range between the turbulent fluctuations due to the dominant mode in the water (mode 1) and those in the gas.

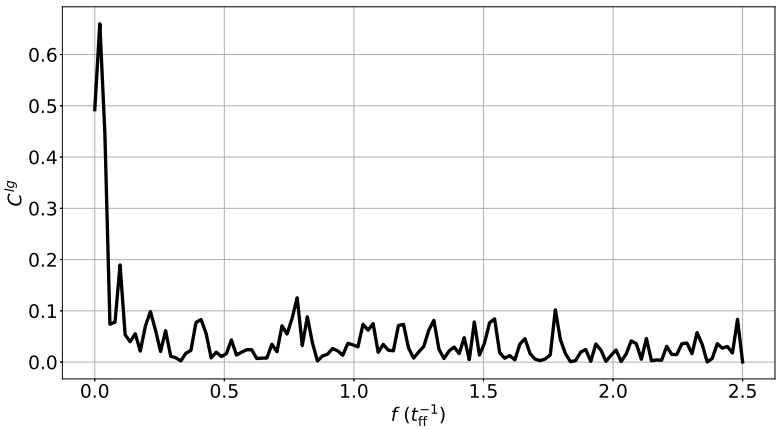

Figure 14: Coherence coefficient C^{lg} between temporal mode 1 of the water and filtered temporal mode 1 of the gas. All frequencies above 0.05 have been removed from the signal of mode 1 of the gas.

Additional evidence can be obtained by applying extended POD in order to extract the part of the gas signal that is directly correlated with the dominant water fluctuation [7]. In the gas, the dominant extended POD mode can be obtained from a linear combination of snapshots where the coefficients of the combination correspond to the POD amplitudes of the dominant water fluctuation. More specifically, the first extended POD mode in the gas, $\boldsymbol{\phi}_1^{ext}$, is computed from equation (25) by using the values in the gas column $\boldsymbol{q}^{g'}(\boldsymbol{x},t^n)$ and the first temporal mode in the water column $A_1^l(t^n)$. In other words,

$$\boldsymbol{\phi}_1^{ext} = \sum_{n=1}^{N} A_1^l(t^n)\boldsymbol{q}^{g'}(\boldsymbol{x},t^n)\,. \tag{32}$$

In figures 15a and 15b we provide color plots of the *normalized* extended mode 1, $\mathbf{\Phi}_1^{ext}$, of the thermal fluctuations in the gas at the two diagonal planes. Upon comparison with the equivalent plots of spatial mode 1 in the gas column, in figures 9a and 9b respectively, we can see that the dominant extended POD displays similar features to the dominant POD mode in the gas column. This observation further reaffirms the strong correlation between the dominant fluctuations in the water and the gas columns.

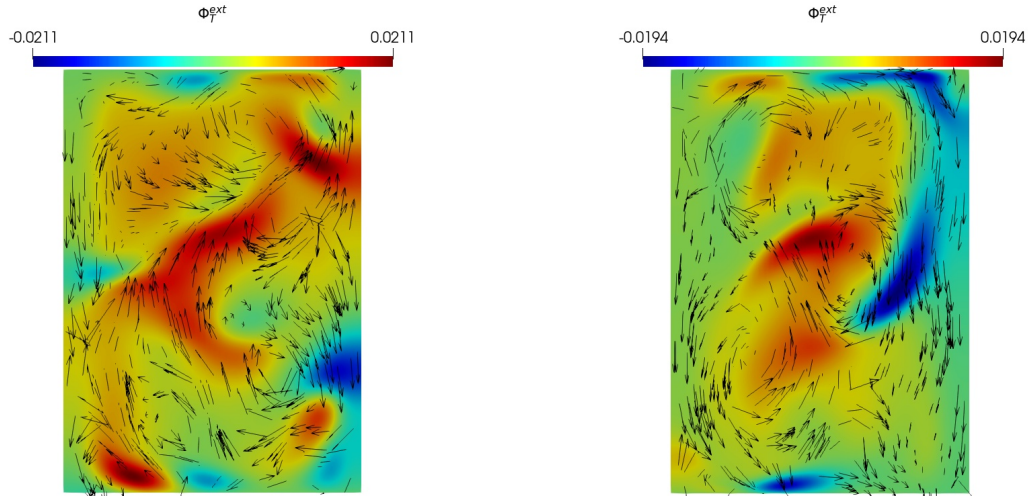

(a) diagonal plane 1, mode 1. **(b)** diagonal plane 2, mode 1.

Figure 15: Extended POD: color plots of the first spatial mode of the thermal fluctuations, superimposed with vector plots of the corresponding velocity modes. (a) diagonal plane 1 (A-C), mode 1. (b) diagonal plane 2 (D-B), mode 1.

5.4. Reconstruction of the flow field

We now discuss the physical meaning of the dominant POD modes in the gas and in the water and their strong coupling observed in the previous section. To this end, we use reconstructions of the instantaneous field using the time-averaged flow and the dominant POD mode.

More specifically, we have reconstructed the fluctuations in the water at $t = 212$, 220 and 240 t_{ff} via equation (21). These time instances have been selected because temporal mode 1 exhibits high peaks at them. Then spatial mode 1 of the fluctuations is added to the time-averaged values in order to reconstruct the instantaneous flow field at these instances. The first spatial modes of the fluctuations in the water and gas columns are denoted by F_1^{l} and F_1^{g}, respectively, and are given by,

$$F_1^{\mathrm{l}} = \sqrt{\lambda_1^{\mathrm{l}}}\Phi_1^{\mathrm{l}}\mathscr{A}_1^{\mathrm{l}}, \qquad \text{and} \qquad F_1^{\mathrm{g}} = \sqrt{\lambda_1^{\mathrm{g}}}\Phi_1^{\mathrm{g}}\mathscr{A}_1^{\mathrm{g}}. \tag{33}$$

In figure 16, we compare the reconstructed streamlines in the water with the instantaneous ones computed via our DNS. The instantaneous streamlines exhibit complicated patterns and are characterized by three impingement points near corners A, D and C at $t = 212$ and 220 t_{ff} and one impingement point near corner D at $t = 240$ t_{ff}. The latter one is due to the main convective roll in diagonal plane 2 whereas the impingement points near corners A and C are due to rolls of smaller size.

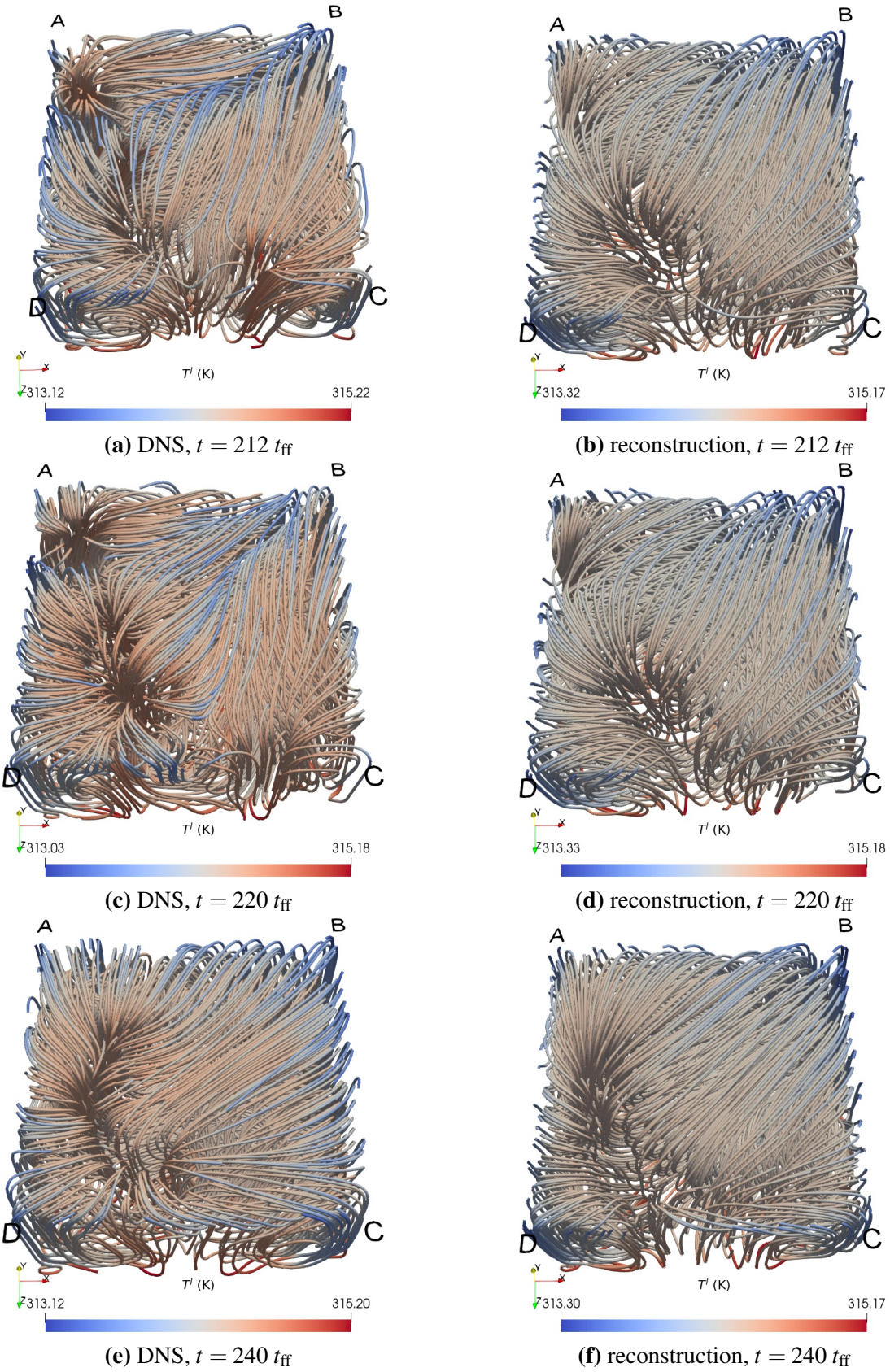

(a) DNS, $t = 212\ t_{\mathrm{ff}}$

(b) reconstruction, $t = 212\ t_{\mathrm{ff}}$

(c) DNS, $t = 220\ t_{\mathrm{ff}}$

(d) reconstruction, $t = 220\ t_{\mathrm{ff}}$

(e) DNS, $t = 240\ t_{\mathrm{ff}}$

(f) reconstruction, $t = 240\ t_{\mathrm{ff}}$

Figure 16: Water column: comparison of instantaneous streamlines from DNS and reconstructed ones from mode 1, at $t = 212$, 220 and 240 t_{ff}. The streamlines are colored with the corresponding instantaneous values of the temperature. Left: top view of DNS results. Right: top view of reconstructed streamlines.

We observe that this reconstruction provides a fairly accurate approximation of the instantaneous streamlines in the water. Further, it predicts accurately the location of the impingement point near corner D at the three time instances considered herein. This allows to conjecture that the evolution of the main convective roll in the water is mostly controlled by mode 1. This is not surprising since the main roll is the largest flow structure and mode 1 has the largest contribution to the POD energy. Additionally, when the amplitude of the first POD mode is positive at $t = 240\ t_{\mathrm{ff}}$ (respectively, negative at $t = 212\ t_{\mathrm{ff}}$ and $t = 220\ t_{\mathrm{ff}}$), it can be shown that the extent of the convection roll is longer (respectively, shorter). Due to the continuity of shear stresses across the free surface and the strong correlation between temporal modes 1 in the two phases, it is expected the size of the bottom roll in the gas to follow these same variations. In other words, the bottom roll in the gas domain becomes shorter at $t = 212 t_{\mathrm{ff}}$.

However, the reconstructed flow fields based on mode 1 do not capture the impingement points near corners A and C. This implies that these features are due to a different mode. In order to determine the modes responsible for them, we have computed two additional reconstructed flow fields at $t = 212\ t_{\mathrm{ff}}$, using the first 5 and the first 10 spatial modes, respectively. Plots of the instantaneous streamlines obtained from these two reconstructed fields are provided in figure 17. According to this figure, the first 5 modes do not contribute to the impingement points near corners A and C even though they contain the vast majority of the POD energy. On the other hand, the main roll which impinges on the free surface near corner D is accurately reconstructed. As explained above, the length of the main roll, i.e. its extent in the diagonal D-B, is affected by mode 1. Additionally, we can notice that in the reconstruction with the first five modes, the streamlines of the main rolls become aligned in the z axis, as in the DNS results. We have confirmed that this rotation of the streamlines is due to mode 2. More specifically, a positive value of temporal mode 2 makes these streamlines rotate counterclockwise, from D towards C. On the contrary, a negative value of mode 2 makes these streamlines rotate clockwise, from D towards A.

Further the reconstructed streamlines based on the first 10 modes do capture these impingement points. This in turn indicates that the vortical structures that impinge on the free surface at corners A and C are associated with low-energy modes (modes 6 to 10) and, therefore, represent a small part of the turbulent kinetic energy in the water column.

The same procedure, *i.e.* adding spatial mode 1 to the time-averaged quantities, is used for the reconstruction of the flow field in the gas column. In figure 18 we present color plots of the instantaneous temperature distribution at the two diagonal planes and at $t = 212 t_{\mathrm{ff}}$, superimposed with vector plots of the velocity.

The DNS results are shown in figures 18a and 18b and the reconstructed fields in figures 18c and 18d. Upon comparison, we deduce that this reconstruction provides a good approximation of the instantaneous flow field. In particular, it captures accurately the inner dual-roll structure, the upward and downward

plumes and the thermal boundary layers at the boundaries. The good agreement between reconstructed fields and DNS results is not surprising because mode 1 represents half of the fluctuations of the flow variables and the value of $\mathscr{A}_1^{\mathrm{g}}$ at $t = 212\,t_{\mathrm{ff}}$ is quite high.

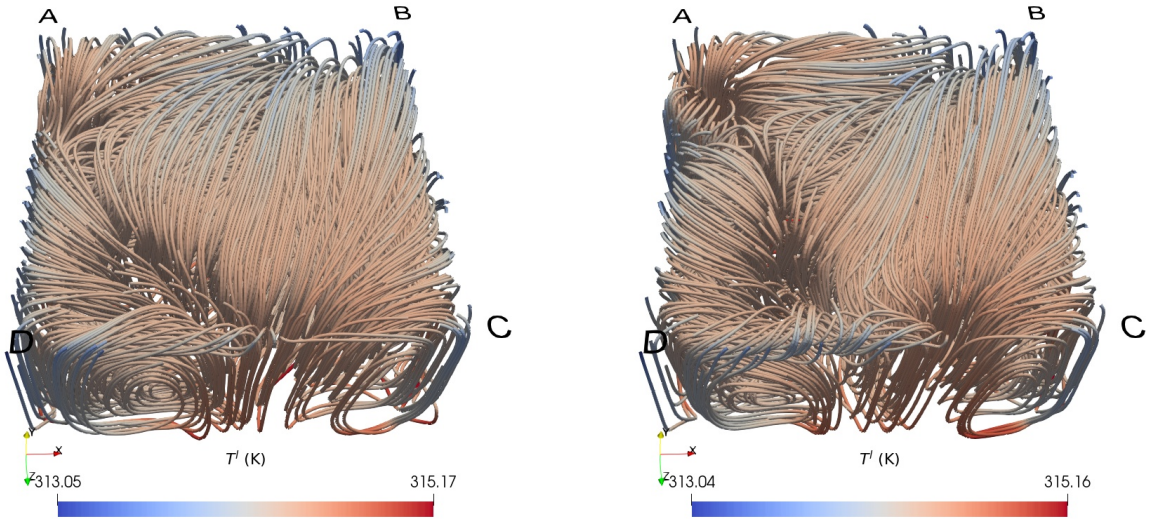

(a) modes 1–5 **(b)** modes 1–10

Figure 17: Water column: top view of reconstructed instantaneous streamlines at $t = 212\,t_{\mathrm{ff}}$. The streamlines are colored by the instantaneous values of the reconstructed temperature field. (a) reconstruction with modes 1–5. (b) reconstruction with modes 1–10.

Comparison of the instantaneous and the time-averaged field in figure 5 shows that the effect of the first mode contribution is to decrease the extent of the lower roll, while increasing that of the higher roll. This observation is consistent with the effect of modes 1 in the two phases at $t = 212\,t_{\mathrm{ff}}$ discussed above. In order to get a better idea of the effect of spatial mode 1 we have also performed a "reverse reconstruction", according to which the mode is subtracted from the time-averaged fields. In other words, we have performed a reconstruction with the sign of $\mathscr{A}_1^{\mathrm{g}}$ been reversed. The results of this procedure are shown in figures 18e and 18f. The rolls of the dual-roll structure in diagonal plane 2 are marked with white circles in figures 18d and 18f. We can observe that in the reverse reconstruction (figure 18f) the size of the lower roll has increased and that of the upper roll has decreased. Consequently, the lower roll has now become the largest one. Whereas, according to the DNS results (figure 18d), the upper roll is in fact the largest one. Also the reverse reconstruction gives a narrower separation between the two interior rolls in diagonal plane 2. Further, comparison of the DNS results with the reverse reconstruction reveals visible differences in the direction of the velocity vectors and in the temperature distribution in the bulk of the gas column. For example, the reverse reconstruction predicts higher temperatures therein, especially in diagonal plane 1.

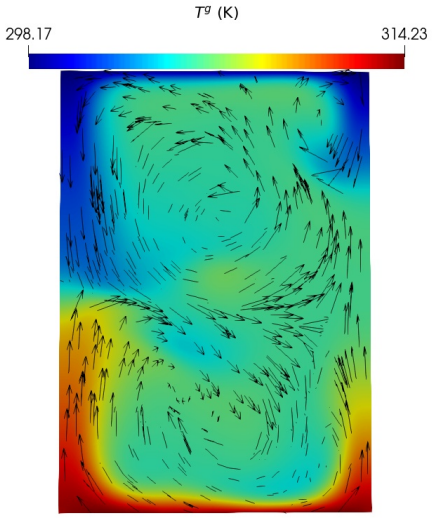

(a) diagonal plane 1, DNS.

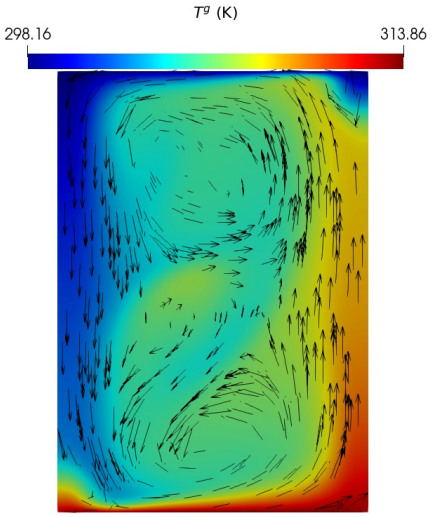

(b) diagonal plane 2, DNS.

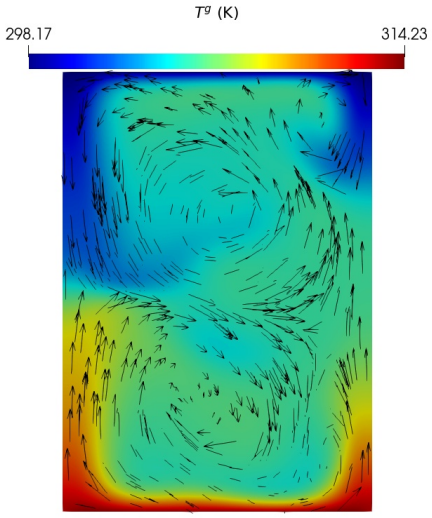

(c) diagonal plane 1, reconstruction.

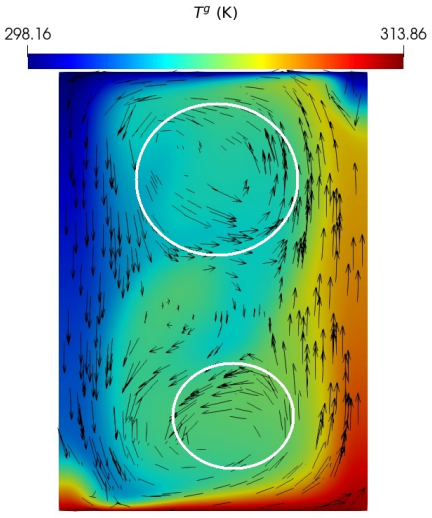

(d) diagonal plane 2, reconstruction.

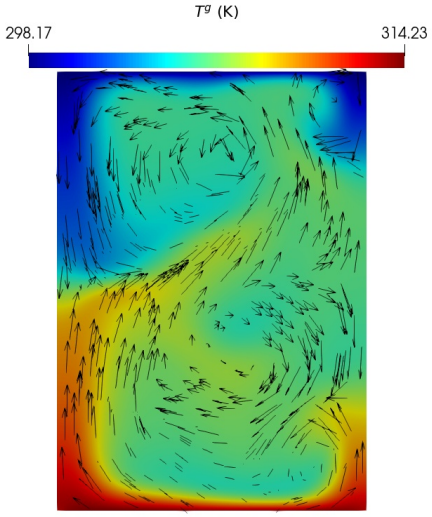

(e) diagonal plane 1, reverse reconstruction.

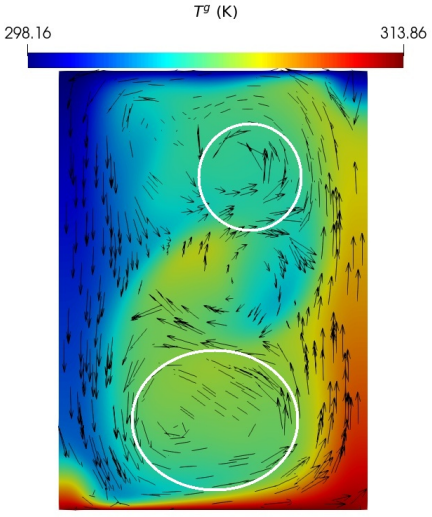

(f) diagonal plane 2, reverse reconstruction.

Figure 18: Gas column: color plots of the instantaneous temperature distribution at $t = 212\,t_{\rm ff}$ and superimposed vector plots of the velocity field. (a)-(b) DNS results. (c)-(d) reconstructed field with mode 1. (e)-(f) reverse reconstruction (subtraction of mode 1 from the time-averaged field). The white circles in figures (d) and (f) mark the location and size of the rolls comprising the dual-roll structure.

On the other hand, the reverse reconstruction has not modified the direction of rotation of the large convective rolls of the flow field, or the structures of the boundary layers. This implies that the main effect of spatial mode 1 is on the dual-roll structure. For example, the difference between the size of the upper and lower rolls is attributed to mode 1. Furthermore, since this dual-roll structure is present in both the time-averaged and the fluctuating flow fields, we deduce that the fluctuations due to mode 1 are not sufficiently strong to break this structure.

As a side note, it is worth adding that the instantaneous temperature and velocity fields $t = 212 t_{\rm ff}$ bear certain similarities with the time-averaged results (shown in figure 5), especially with regard to the structure of the large vortical structures. Nonetheless, there are some differences too; the most noticeable ones relate to the direction of the currents and the details of the temperature distribution in the bulk.

With the aim of investigating further the effect of the first spatial mode in the gas column, we have computed the angular momentum $\boldsymbol{L} = (L_x, L_y, L_z)$ of each horizontal layer of cells with respect to the center $\boldsymbol{x}_0$ of the layer, $\boldsymbol{x}_0 = (W/2, y, W/2)$. Accordingly, $\boldsymbol{L}$ is defined by

$$\boldsymbol{L} = \int_{V_h} (\boldsymbol{x} - \boldsymbol{x}_0) \wedge \rho \boldsymbol{u} \, dV \,, \tag{34}$$

where V_h is the total volume of the horizontal layer of cells. It is noted that this definition is different from the classical one, where a single reference point is used.

In figure 19, we provide plots of the y component of the angular momentum of the layers. This corresponds to the torsion of the fluid at xz planes with respect to the centerline, *i.e.* the y axis at mid-width. More specifically, in this figure we have plotted the time-averaged profile of the torsion $L_y(\langle \rho \boldsymbol{u} \rangle_t)$, the torsion $L_y(F_1^{\rm g})$ associated with spatial mode 1 at $t = 212 t_{\rm ff}$, and their sum. We observe that $L_y(\langle \rho \boldsymbol{u} \rangle_t)$ assumes an S-shaped profile and its amplitude is characterized by two peaks that correspond to the two principal rolls of the large-scale circulation. On the other hand, its profile is not symmetric with respect to the mid-height of the gas column; for example, the top peak is higher than the lower one. Also, $L_y(\langle \rho \boldsymbol{u} \rangle_t)$ vanishes (is zero) at the free surface whereas it attains a non-zero value at the open-top boundary. This asymmetry is attributed to the difference of the shear stresses at these two planes. More specifically, the open-top boundary is shear-free. Whereas the free surface supports shear stresses which tend to constrain the motions of the gas above it. Another interesting observation in figure 19 is that the torsion due to the first spatial mode reinforces the time-averaged torsion throughout the gas column.

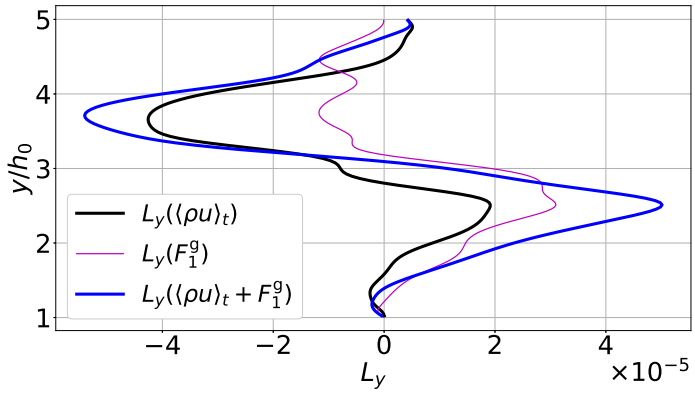

Figure 19: Plots of the y component of the angular momentum (torsion). The profile due to spatial mode 1 is taken at $t = 212 t_{\rm ff}$.

Finally, the x and z components of the angular momentum, are presented in figure 20. As before, in this figure we have plotted the time-averaged profile, the profile due to spatial mode 1 at $t = 212 t_{\rm ff}$ and their sum. According to them, the time-averaged profiles are everywhere positive and are characterized by two peaks. However, their order is reversed in the x and z components: in the x component the lower peak is the highest one while the opposite holds true for the z component. Further, spatial mode 1 reinforces the angular momentum in the upper part of the gas column since both $L_x(F_1^{\rm g})$ and $L_z(F_1^{\rm g})$ components of it are positive therein. On the other hand, it tends to reduce it in the lower part, because $L_x(F_1^{\rm g})$ and $L_z(F_1^{\rm g})$ are negative. As a result, the sum of the two contributions (time-averaged and the one related to mode 1) attains higher values in the upper part than in the lower one. This is in accordance with the observation made above that, in the gas column and at this particular time, the upper roll becomes predominant.

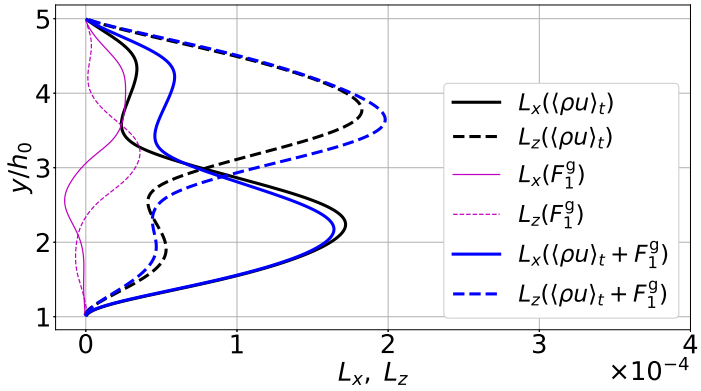

Figure 20: Plots of the x and z components of the angular momentum. The profile due to spatial mode 1 is taken at $t = 212 t_{\rm ff}$.

6. Conclusions

In this paper, we analyzed the turbulent structures during natural convection of water and air in a pool with evaporation across the free surface. In the water, the time-averaged flow consists of a large convective roll aligned in one of the diagonals. While in the air the flow is organized in complex pattern consisting of an inner dual-roll structure with wall-parallel orthogonal axes and an outer circulation aligned in the same diagonal plane as the large roll of water.

In order to calculate appropriately the energy of the fluctuations in each phase, we have performed separate PODs in the water and gas columns. According to our analysis, the spectrum of the fluctuations in the water is characterized by a single low-frequency peak that corresponds to the recirculation frequency of the mean roll. In contrast, the spectrum in the air is bimodal, with a high-frequency peak that can be attributed to recirculation motions associated with the dual-roll structure, and a low-frequency modulation that matches that of the water. Despite this complexity, POD analysis showed that the fluctuations are more coherent in the gas than in the water. More specifically, in the gas the fluctuations were strong at mid-height and in the regions of strong-shear that connect the two convective rolls. While in the water, the most energetic POD modes can be well tracked through the interface, where a key feature is the location of the main impingement point.

To investigate the connection between the fluctuations in the water and in the gas, we determined which POD modes in the air were best correlated with the dominant POD modes in the water. It was established that the most energetic fluctuation in the air was well correlated with the dominant water fluctuation.

Further, we have reconstructed the flow field in each column by using the corresponding dominant POD modes. It was shown that the superposition of the time-averaged field with those due to the first spatial modes can yield reasonable approximations of the instantaneous distributions of the flow variables. In particular, such a reconstruction captures well the instantaneous realizations of the large-scale circulations in the two phases. It was observed that, in the water, the main effect of the dominant mode is to modify the size of the mean convective roll. Nonetheless, the dominant mode does not affect its orientation. Additionally, a reduced convective roll in the water is associated with a weaker bottom roll in the air, and a stronger top roll. The second most energetic mode in the water is also associated with a displacement of the main impingement point, but in a direction orthogonal to that of the main roll.

This study was based on a single pair of initial Rayleigh numbers for the water and gas columns, Ra^l and Ra^g. The values considered herein (at the order of 10^6) are representative of natural convection at weak to moderate turbulence intensities. Accordingly, the turbulent structures and flow properties predicted by our study are expected to be relevant for natural convection in this regime. Evidently, at higher Rayleigh numbers the organization of the flow might be different. Nonetheless, certain characteristics,

such as the bimodality of the spectra of the fluctuations and temporal modes in the gas and the correlation between the large-scale circulations in the two phases, are due to the interaction between the two phases at the free surface. This suggests that these characteristics are intrinsic to the dynamics of the two-phase system and that they are present even at high turbulence intensities. Finally, it is interesting to mention that no flow reorientations were predicted in our simulation. Although such phenomena are expected to be hampered by the low aspect ratio of the gas column and the gas-water interaction, more studies would be needed to determine whether they occur in a different range of Rayleigh numbers.

Acknowledgments

The first and third authors gratefully acknowledge the financial support provided by the Belgian Federal Public Service Economy under the Energy Transition Fund, project SFP-LOCA.

Declaration of Competing Interest

The authors declare no conflict of interest.

Author Contribution

J. Carlier: conceptualization, methodology, software, validation, investigation, formal analysis, data curation, visualization, writing (original draft, review and editing).

B. Podvin: conceptualization, methodology, investigation, formal analysis, writing (original draft, review and editing).

M.V. Papalexandris: conceptualization, investigation, resources, writing (original draft, review and editing), project administration, funding acquisition.

References

[1] Ahlers, G., Bodenschatz, E., Hartmann, R., He, X., Lohse, D., Reiter, P., Stevens, R., Verzicco, R., Wedi, M., Weiss, S., et al., 2022. Aspect ratio dependence of heat transfer in a cylindrical Rayleigh-Bénard cell. Phys. Rev. Lett. 128, 084501.

[2] Antoniadis, P.D., Papalexandris, M.V., 2016. Numerical study of unsteady, thermally-stratified shear flows in superposed porous and pure-fluid domains. Int. J. Heat Mass Tran. 96, 643–659.

[3] Bailon-Cuba, J., Emran, M.S., Schumacher, J., 2010. Aspect ratio dependence of heat transfer and large-scale flow in turbulent convection. J. Fluid Mech. 655, 152–173.

[4] Bailon-Cuba, J., Schumacher, J., 2011. Low-dimensional model of turbulent Rayleigh-Bénard convection in a Cartesian cell with square domain. Phys. Fluids 23, 077101.

[5] Barta, R., Wagner, C., 2025. Large-scale reorientation in cubic Rayleigh–Bénard convection measured with particle tracking velocimetry. J. Turbul. 26, 36–49.

[6] Berkooz, G., Holmes, P., Lumley, J.L., 1993. The proper orthogonal decomposition in the analysis of turbulent flows. Annu. Rev. Fluid Mech. 25, 539–575.

[7] Boree, J., 2003. Extended proper orthogonal decomposition: a tool to analyse correlated events in turbulent flows. Exp. Fluids 35, 188–192.

[8] Brewster, M.Q., 2018. Evaporation of water at high mass-transfer rates by natural convection air flow with application to spent-fuel pools. Int. J. Heat Mass Tran. 116, 703–714.

[9] Buevich, Y., Mankevich, V., 1989. Natural thermal-concentration convection. J. Eng. Phys. Thermophys. 57, 1277–1284.

[10] Carlier, J., Papalexandris, M.V., 2023. An efficient tracking method of evaporative and flat free surfaces for turbulent convection. Comput. Fluids 257, 105882.

[11] Carlier, J., Papalexandris, M.V., 2024. Turbulent natural convection in an airâĂŞwater system with evaporation across the free surface. Int. J. Multiphas. Flow 177, 104873.

[12] Chu, B.T., 1965. On the energy transfer to small disturbances in fluid flow (Part I). Acta Mech. 1, 215–234.

[13] Deacon, E.L., 1977. Gas transfer to and across an air-water interface. Tellus 29:4, 363–374.

[14] Deane, A.E., Sirovich, L., 1991. A computational study of Rayleigh–Bénard convection. Part 1. Rayleigh-number scaling. J. Fluid Mech. 222, 231–250.

[15] Druault, P., Bouhoubeiny, E., Germain, G., 2012. POD investigation of the unsteady turbulent boundary layer developing over porous moving flexible fishing net structure. Exp. Fluids 53, 277–292.

[16] Georgiou, M., Papalexandris, M.V., 2017. Turbulent mixing in T-junctions: The role of the temperature as an active scalar. Int. J. Heat Mass Tran. 115, 793–809.

[17] Grötzbach, G., 1983. Spatial resolution requirements for direct numerical simulation of the Rayleigh-Bénard convection. J. Comput. Phys. 49, 241–264.

[18] Hay, W.A., Martin, J., Migot, B., Papalexandris, M.V., 2021. Turbulent thermal convection driven by free-surface evaporation in cuboidal domains of different aspect ratios. Phys. Fluids 33, 015104.

[19] Hay, W.A., Papalexandris, M.V., 2019. Numerical simulations of turbulent thermal convection with a free-slip upper boundary. Proc. Roy. Soc. A-Math. Phys. 475, 20190601.

[20] Hay, W.A., Papalexandris, M.V., 2020. Evaporation-driven turbulent convection in water pools. J. Fluid Mech. 904, A14.

[21] He, X., van Gils, D.P.M., Bodenschatz, E., Ahlers, G., 2014. Logarithmic spatial variations and universal f-1 power spectra of temperature fluctuations in turbulent Rayleigh-Bénard convection. Phys. Rev. Lett. 112, 174501.

[22] Jing, C.J., Henry, D., Hadid, H.B., Imaishi, N., 2003. Low-order dynamical model for low-Prandtl number fluid flow in a laterally heated cavity. Phys. Fluids 15, 2152–2162.

[23] Juric, D., Tryggvason, G., 1998. Computations of boiling flows. Int. J. Multiphas. Flow 24, 387–410.

[24] Karhunen, K., 1946. Zur Spektraltheorie stochastischer Prozesse. Ann. Acad. Sci. Fennicae, AI 34.

[25] Lemmon, E.W., Huber, M.L., McLinden, M.O., 2010. Standard reference database 23: reference fluid thermodynamic and transport properties. Technical Report. NIST. REFPROP, 9th edition.

[26] Lessani, B., Papalexandris, M.V., 2006. Time-accurate calculation of variable-density flows with strong temperature gradients and combustion. J. Comput. Phys. 212, 218–246.

[27] Li, J., Zhang, T., Sun, S., Yu, B., 2019. Numerical investigation of the POD reduced-order model for fast predictions of two-phase flows in porous media. Int. J. Numer. Methods. H. 29, 4167–4204.

[28] Liu, H.R., Chong, K.L., Wang, Q., Ng, C.S., Verzicco, R., Lohse, D., 2021. Two-layer thermally driven turbulence: mechanisms for interface breakup. J. Fluid Mech. 913, A9.

[29] Liu, H.R., Chong, K.L., Yang, R., Verzicco, R., Lohse, D., 2022. Heat transfer in turbulent Rayleigh-Bénard convection through two immiscible fluid layers. J. Fluid Mech. 938, A31.

[30] Loève, M., 1945. Sur les fonctions aléatoires stationnaires du second ordre. Revue Scientifique 83, 297–303.

[31] Lumley, J.L., 1967. The structure of inhomogeneous turbulence, in: Yaglom, A.M., Tatarski, V.I. (Eds.), Atmospheric Turbulence and Radio Wave Propagation, Nauka. pp. 166–178.

[32] Lumley, J.L., 1981. Coherent structures in turbulence, in: Meyer, R.E. (Ed.), Transition and Turbulence, Elsevier. pp. 215–242.

[33] Lumley, J.L., Poje, A., 1997. Low-dimensional models for flows with density fluctuations. Phys. Fluids 9, 2023–2031.

[34] Marichal, J., Papalexandris, M.V., 2022. On the dynamics of the large scale circulation in turbulent convection with a free-slip upper boundary. Int. J. Heat Mass Tran. 183C, 122220.

[35] Marrero, T., Mason, E., 1972. Gaseous diffusion coefficients. J. Phys. Chem 1, 3–118.

[36] Martin, J., Migot, B., American Nuclear Society, Portland, Oregon, 2019. Experimental study of the surface evaporation rate of a heated water pool at high temperature using infrared thermography. 18th International Topical Meeting on Nuclear Reactor Thermal Hydraulics , 2302–2313.

[37] Munir, S., Siddiqui, M.I., Aziz, A.R.B.A., Heikal, M., Farooq, U., 2022. Proper orthogonal decomposition based on vorticity: Application in a two-phase slug flow. J. Fluid Eng. 144, 041501.

[38] Munir, S., Siddiqui, M.I., Heikal, M., Aziz, A.R.A., de Sercey, G., 2015. Identification of dominant structures and their flow dynamics in the turbulent two-phase flow using POD technique. J. Mech. Sci. Technol. 29, 4701–4710.

[39] Niemela, J.J., Skrbek, L., Sreenivasan, K.R., Donnelly, R.J., 2000. Turbulent convection at very high Rayleigh numbers. Nature 404, 837–840.

[40] Pang, M., Wei, J., 2013. Experimental investigation on the turbulence channel flow laden with small bubbles by PIV. Chem. Eng. Sci. 94, 302–315.

[41] Paolucci, S., 1982. Filtering of sound from the Navier–Stokes equations. NASA STI/Recon Technical Report N 83, 26036.

[42] Papalexandris, M.V., 2020. On the applicability of Stokes' hypothesis to low-Mach-number flows. Continuum Mech. Therm. 32, 1245–1249.

[43] Park, H.M., Sung, M.C., Chung, J.S., 2004. Stabilization of Rayleigh–Bénard convection by means of mode reduction. Prox. Roy. Soc. A-Math. Phy. , 1807–1830.

[44] Podvin, B., Le Quéré, P., 2001. Low-order models for the flow in a differentially heated cavity. Phys. Fluids 13, 3204–3214.

[45] Podvin, B., Sergent, A., 2012. Proper orthogonal decomposition investigation of turbulent Rayleigh-Bénard convection in a rectangular cavity. Phys. Fluids 24, 105106.

[46] Podvin, B., Sergent, A., 2015. A large-scale investigation of wind reversal in a square Rayleigh–Bénard cell. J. Fluid Mech. 766, 172–201.

[47] Podvin, B., Sergent, A., 2017. Precursor for wind reversal in a square Rayleigh-Bénard cell. Phys. Rev. E 95, 013112.

[48] Scapin, N., Demou, A.D., Brandt, L., 2023. Evaporating Rayleigh-Bénard convection: prediction of interface temperature and global heat transfer modulation. J. Fluid Mech. 957, A12.

[49] Schmidt, O.T., Colonius, T., 2020. Guide to spectral proper orthogonal decomposition. AIAA J. 58, 1023–1033.

[50] Shishkina, O., Stevens, R., Grossmann, S., Lohse, D., 2010. Boundary layer structure in turbulent thermal convection and its consequences for the required numerical resolution. New. J. Phys. 12, 075022.

[51] Sirovich, L., 1987. Turbulence and the dynamics of coherent structures; part I: coherent structures. Q. Appl. Math. 45, 561–571.

[52] Slattery, J., 1999. Advanced Transport Phenomena. Cambridge University Press.

[53] Smith, T.R., Moehlis, J., Holmes, P., 2005. Low-dimensional modelling of turbulent using the proper orthogonal decomposition: a tutorial. Nonlinear Dynam. 41, 275–307.

[54] Soucasse, L., Podvin, B., Rivière, P., Soufiani, A., 2019. Proper orthogonal decomposition analysis and modelling of large-scale flow reorientations in a cubic Rayleigh–Bénard cell. J. Fluid Mech. 881, 23–50.

[55] Soucasse, L., Podvin, B., Rivière, P., Soufiani, A., 2021. Low-order models for predicting radiative transfer effects on Rayleigh–Bénard convection in a cubic cell at different Rayleigh numbers. J. Fluid Mech. 917, A5.

[56] Spangenberg, W.G., Rowland, W.R., 1961. Convective circulation in water induced by evaporative cooling. Phys. Fluids 4, 743–750.

[57] Stevens, R., Verzicco, R., Lohse, D., 2010. Radial boundary layer structure and Nusselt number in Rayleigh-Bénard convection. J. Fluid Mech. 643, 495–507.

[58] Taira, K., Brunton, S.L., Dawson, S.T.M., Rowley, C.W., Colonius, T., McKeon, B.J., Schmidt, O.T., Gordeyev, S., Theofilis, V., Ukeiley, L.S., 2017. Modal analysis of fluid flows: An overview. AIAA J. 55, 4013–4041.

[59] Tanguy, S., Ménard, T., Berlemont, A., 2007. A level set method for vaporizing two-phase flows. J. Comput. Phys. 221, 837–853.

[60] Tennekes, H., Lumley, J., 1972. A first course in turbulence. MIT press.

[61] Verdoold, J., Tummers, M.J., Hanjalić, K., 2009. Prime modes of fluid circulation in large-aspect-ratio turbulent Rayleigh-Bénard convection. Phys. Rev. E 80, 037301.

[62] Weiss, J., 2019. A Tutorial on the Proper Orthogonal Decomposition, in: AIAA 2019 Aviation Forum.

[63] Yi, S.J., Kim, S.M., Kim, H.D., Kim, J.W., Kim, K.C., 2010. Spatial and temporal structures of turbulent bubble-driven flows in a rectangular water tank. J. Mech. Sci. Technol. 24, 1819–1827.

[64] Zhang, L., Chong, K.L., Xia, K.Q., 2019. Moisture transfer by turbulent natural convection. J. Fluid Mech. 874, 1041–1056.

[65] Zikanov, O., Slinn, D.N., Dhanak, M.R., 2002. Turbulent convection driven by surface cooling in shallow water. J. Fluid Mech. 464, 81–111.